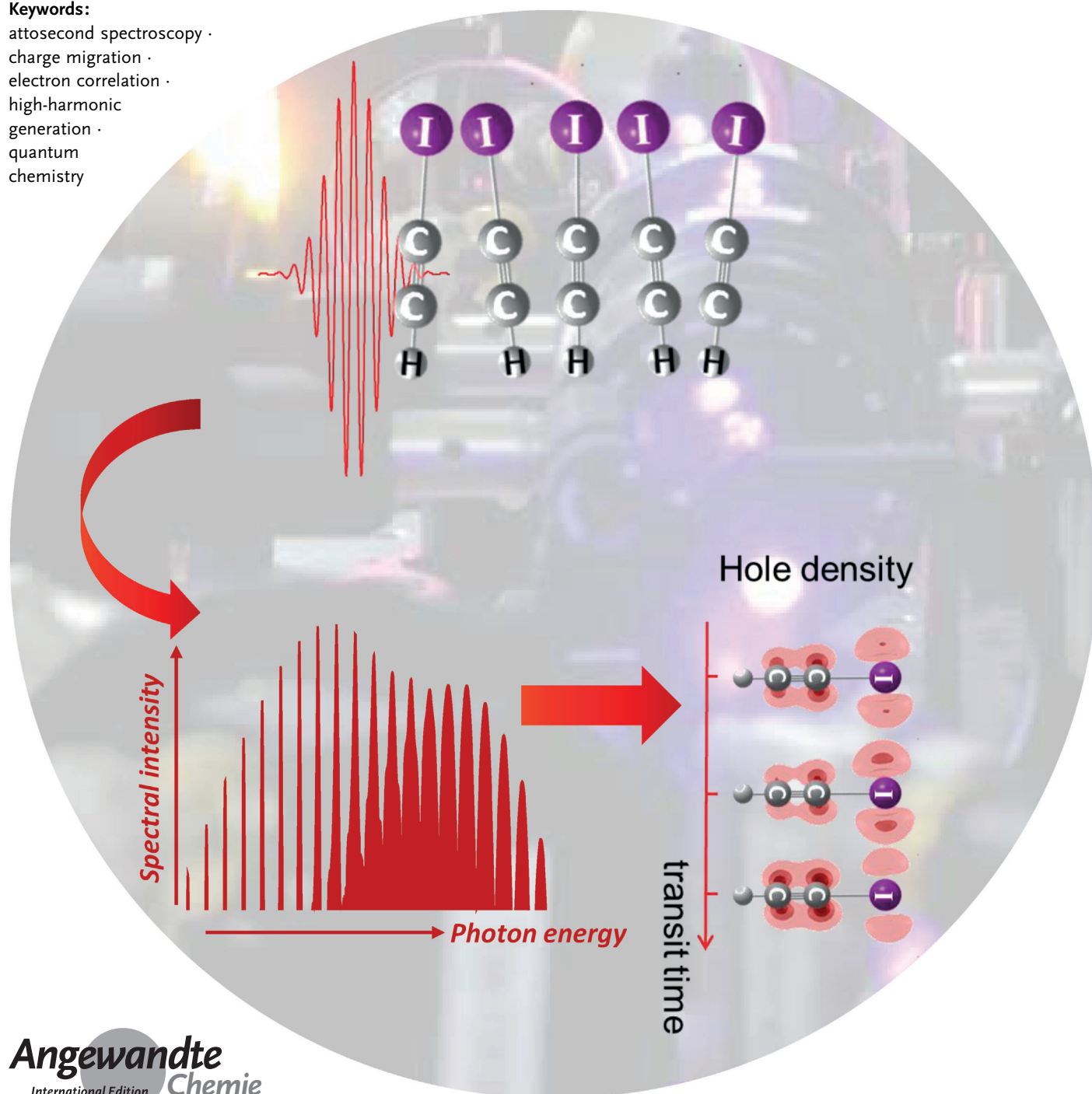


Perspectives of Attosecond Spectroscopy for the Understanding of Fundamental Electron Correlations

Peter M. Kraus* and Hans Jakob Wörner*

Keywords:

attosecond spectroscopy ·
charge migration ·
electron correlation ·
high-harmonic
generation ·
quantum
chemistry



The description of the electronic structure of molecules in terms of molecular orbitals is a highly successful concept in chemistry. However, it commonly fails if the electrons in a molecule are strongly correlated and cannot be treated as independent particles. Electron correlation is essential to understand inner-valence X-ray spectroscopies, it can drive ultrafast charge migration in molecules, and it is responsible for many exotic properties of strongly correlated materials. Time-resolved spectroscopy with attosecond resolution is generally capable of following electronic motion in real time and can thus provide experimental access to electron-correlation-driven phenomena. High-harmonic spectroscopy in particular uses the precisely timed laser-driven recollision of electrons to interrogate the electronic structure and dynamics of the investigated system on a sub-femtosecond timescale. In this Review, the capabilities of high-harmonic spectroscopy to follow electronic motion in molecules are discussed. Both qualitative and quantitative approaches to unraveling the detailed dynamical responses of molecular systems following ionization are presented. A new theoretical formalism for the reconstruction of correlation-driven charge migration is introduced. The importance of electron–ion entanglement and electronic coherence in the reconstruction of attosecond hole dynamics are discussed. These advances make high-harmonic spectroscopy a promising technique to decode fundamental electron correlations and to provide experimental data on the complex manifestations of multi-electron dynamics.

1. Introduction

1.1. Time-Resolved Electronic Spectroscopy

Electron correlation is one of the central concepts in chemistry as well as in atomic, molecular, and solid-state physics. The term “electron correlation” collectively describes the interaction and mutual influence of electrons within a physical system (for example, an isolated atom or molecule, a liquid, or a solid), which go beyond the description of one electron embedded in the mean field of all remaining electrons.^[1] Generally, the mutual influence of electrons becomes more pronounced with an increasing density of electronic states. Therefore, correlation-dominated effects are always present for inner-valence electrons and are relevant to the interpretation of experiments investigating these electrons, such as X-ray photoelectron spectroscopy.^[2,3] However, outer-valence-shell electrons can also be subject to pronounced electron-correlation effects.^[4,5] This will be the main topic of this Review, because chemical processes are generally dominated by the outermost electrons.

The dynamics of valence electrons on sub-100 fs timescales play important roles in many chemically relevant systems. Charge transfer after photoexcitation was found to create long-lived electronic coherences, which were observed in photosynthetic systems^[6] or photovoltaic blends^[7] by multidimensional electronic spectroscopy^[8,9] in the visible range of the spectrum. Such coherences have been invoked to

From the Contents

1. Introduction	3
2. Theory	7
3. Signatures of Electron Dynamics in High-Harmonic Spectra of Atoms and Aligned Molecules	9
4. Reconstruction of Electron Dynamics from the Observables of High-Harmonic Spectroscopy	12
5. Perspectives for Decoding Electron Correlation by High-Harmonic Spectroscopy	16
6. Conclusions and Outlook	18


explain the high efficiencies of energy conversion in these systems,^[10] even though these interpretations are still debated today.^[11] Attosecond spectroscopy will provide new access to these long-standing problems, contributing attosecond temporal and potentially Ångström spatial resolution. In addition to investigating the role of electronic coherences in biological complexes, photoexcitation can prepare electron circulations in ring-shaped molecules.^[12–14] The magnitude of the unidirectional ring-currents in a single molecule, which can be controlled by the circularity of the light or the chirality of the material, could surpass the available technologies for generating the strongest magnetic fields.^[15] In general, attosecond spectroscopy is expected to contribute to the understanding of the charge flow, which naturally occurs on the fs to sub-fs timescale.

Electron correlation can have a profound influence on electron dynamics.^[16] This motivates the application of time-resolved spectroscopies to track and quantify correlation-driven phenomena. The natural timescale of electron motion lies in the few-femtosecond to attosecond range, which until recently posed major challenges to the available laser

[*] Dr. P. M. Kraus

Department of Chemistry, University of California
Berkeley, California 94720 (USA)
E-mail: peter.kraus@berkeley.edu

Prof. Dr. H. J. Wörner
Laboratorium für Physikalische Chemie, ETH Zürich
Vladimir-Prelog-Weg 2, 8093 Zürich (Switzerland)
E-mail: hwoerner@ethz.ch
Homepage: <http://www.atto.ethz.ch>

 The ORCID identification number(s) for the author(s) of this article can be found under:
<https://doi.org/10.1002/anie.201702759>.

technologies. However, the discovery of high-harmonic generation (HHG), the up-conversion of many infrared photons into one extreme-ultraviolet (XUV) photon through a highly nonlinear interaction of intense laser pulses with a gas, enabled the generation and characterization of attosecond pulse trains^[17] and isolated attosecond pulses.^[18]

Examples of few- to subfemtosecond timescale experiments employing attosecond pulses to monitor ultrafast electronic processes are numerous and have been reviewed several times.^[19–24] Employing isolated attosecond pulses^[18] interatomic decay processes such as Auger decays in atoms could be measured in real-time by attosecond photoelectron^[25] and photoion techniques.^[26] Electronic dynamics in highly excited states of atoms and molecules could be resolved through a combination of attosecond XUV ionization or excitation and the subsequent interaction with an infrared pulse. Attosecond XUV transient absorption experiments measured the lifetimes of excited autoionizing states in atoms^[27,28] and characterized two-electron wave packets in excited states of helium.^[29] Photofragmentation techniques revealed the short-time dynamics of molecular hydrogen after attosecond XUV photoionization.^[30] Ultrafast charge motion in the phenylalanine cation^[31–34] could be initiated by attosecond XUV photoionization, which populates a broad distribution of excited states in the molecular cation, and subsequently probed by infrared multiphoton ionization.

Electronic dynamics in the valence shell of atoms and molecules can be initiated through ionization or excitation to excited states of the neutral species. Strong-field ionization (SFI) was used to prepare valence electron motion in the two lowest-lying spin-orbit states of the krypton cation.^[35,36] The evolution of the hole density could be followed by element-specific attosecond transient-absorption spectroscopy.^[36] Other ways of probing SFI-initiated dynamics is ionization to the dication, which was used to follow the spin-orbit wave packets in the neon, argon, and hydrogen chloride (HCl) cations.^[37–39] Alternatively, electronic coherences in neutral molecules can be prepared by impulsive stimulated Raman scattering (ISRS) and followed by a second time-delayed pulse, which generates high harmonics from the coherent superposition of states,^[40–42] or by strong-field ionization and holography.^[159]

All experiments described in this section employ pump-probe schemes for following electronic dynamics in atoms and molecules. They have all remained limited to the few-femtosecond timescale because of the necessity of a near-infrared pulse as either the pump or probe. An alternative approach for measuring attosecond dynamics consists in using the precisely timed attosecond electron bunches generated during strong-field light-matter interactions instead of light pulses with similar durations. This approach improves the temporal resolution to typically about one hundred attoseconds. Examples of experiments employing such attosecond electron bunches are discussed in the next section.

1.2. High-Harmonic Spectroscopy

Many of the strong-field processes underlying attosecond pulse production have been explored as techniques to study attosecond timescale phenomena. One attractive feature of these experiments is the possibility of reaching attosecond temporal resolution without the use of attosecond light pulses.

Around the same time as the first demonstration of isolated attosecond pulses,^[18] the correlation between a vibrational wave packet in H_2^+ prepared by SFI and the associated continuum-electron wave packet was exploited to characterize the temporal structure of the returning electron current by analyzing the kinetic energy of the protons produced by inelastic scattering of the recolliding electron.^[43] Turning the approach around, the correlated nature of the two wave packets could also be used to study the nuclear wave packet motion in D_2^+ by performing measurements with various driving wavelengths.^[44] These experiments paved the way towards performing attosecond timescale experiments with attosecond electron bunches instead of attosecond laser pulses.

The potential of these ideas has been investigated in numerous examples, most notably involving HHG. Within the classical three-step model of HHG,^[45,46] an electron is tunnel-ionized by a strong laser field, subsequently accelerated by the field, and allowed to recombine after the field has reversed its sign. During tunnel ionization, the strong infrared laser field bends the Coulomb binding potential of the



Peter Kraus, born in Marburg in 1988, studied chemistry at Philipps-University Marburg, the University of Helsinki and ETH Zurich. He completed his Ph.D. thesis under the guidance of Prof. Hans Jakob Wörner at ETH Zurich in 2015 on investigations of ultrafast electronic and nuclear dynamics in molecules by high-harmonic spectroscopy. For his thesis he was awarded the ETH medal for outstanding dissertations, and the Justin Jankunas award for the best thesis in chemical physics by the American Physical Society (APS). In 2015 he joined the groups of Prof. Stephen Leone and Prof. Daniel Neumark at the University of California, Berkeley, developing new methods for studying attosecond dynamics in solid-state materials.



Hans Jakob Wörner studied chemistry at the EPF Lausanne and the ETH Zürich. He obtained his Ph.D. degree in 2007 from ETH Zürich under the guidance of Prof. Frédéric Merkt for high-resolution spectroscopic studies of non-Born-Oppenheimer effects. After a short postdoctoral period at the Laboratoire Aimé-Cotton in Orsay, he joined the group of Prof. Paul Corkum at the National Research Council of Canada. In 2010 he returned to ETH Zürich with a SNF professorship and was promoted to a tenured position in 2013. He has received many awards for his work, including the Nernst-Haber-Bodenstein prize of the Bunsen society, the Klung-Wilhelmy Science award of the Freie Universität Berlin, and the Carus Medal of the Deutsche Akademie der Naturforscher Leopoldina.

electron, which allows it to tunnel out.^[47] Tunnel ionization depends exponentially on the electric field amplitude and the ionization potential. Thus tunnel ionization to higher lying states of the cation is strongly suppressed and generally only noticeably occurs in molecules with closely spaced electronically excited states of the cation, which give rise to the complex multielectron dynamics discussed in the following sections. The sub-cycle timing of the electron trajectories in HHG was subsequently identified as a promising approach for achieving attosecond temporal resolution, which was recognized to be suitable for following ultrafast nuclear wave packets created by ionization.^[48] This was realized experimentally shortly after the theoretical proposal through measurements of the proton dynamics in $\text{H}_2^+/\text{D}_2^+$ and $\text{CH}_4^+/\text{CD}_4^+$ initiated by SFI.^[49,50]

Generally, SFI does not prepare an eigenstate of the system, but ionizes to multiple electronically^[51,52,37] and vibrationally^[53] excited states of the cation; that is, SFI can launch electronic as well as nuclear dynamics. Owing to the sub-cycle timing of the electron trajectories in the laser field (Figure 1a), every harmonic order can be associated with a well-defined time that the electron has spent in the continuum (Figure 1b), thus providing an intrinsic attosecond delay line. Photorecombination finally probes the dynamics. Performing such measurements at wavelengths different from the standard titanium:sapphire wavelength of 800 nm, for example, 1300 nm (Figure 1c,d), opens different transit-time windows, that is, different time delays between SFI (pump) and photorecombination (probe).^[54–56] The unique mapping between photon energies and transit times is not only a theoretical result (next section), it has also been verified experimentally in the reconstruction of attosecond beating by interference of two-photon transitions (RABBIT)^[57] as well as two-color HHG experiments.^[58–60]

Simultaneously, high-harmonic spectroscopy (HHS) was explored as a method for broadband measurements of the electronic structure. This approach relies on the conceptual similarity between single-photon photoionization and photorecombination. Pioneering work revealed the dependence of HHG on the molecular alignment^[61–63] and was utilized for the tomographic reconstruction of molecular orbitals^[62,64–67] using the plane-wave approximation. The plane-wave approximation was, however, questioned, when signatures known from photoionization cross-sections were identified in HHG spectra.^[68–70] These results revealed the importance of a correct description of the photoionization continuum beyond the plane-wave approximation. Examples include the electronic structure minimum in argon^[69] and the giant resonance in xenon,^[71,72] both of which are discussed in this Review, as well as further studies of Cooper minima^[73,74] and shape resonances^[73,75–78] in molecules.

Combining the ideas of attosecond temporal resolution and sensitivity to electronic structure, investigations of attosecond electron dynamics launched by SFI were triggered by the observation of spectral intensity minima in

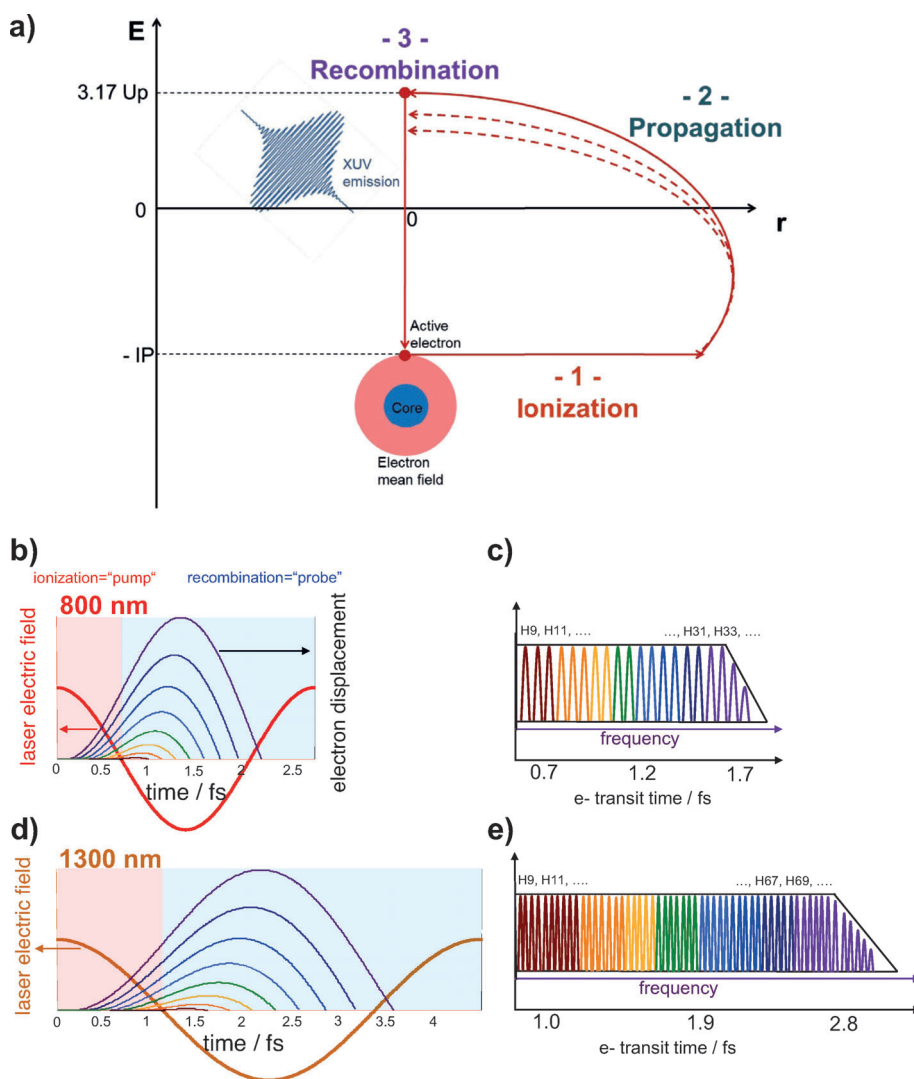


Figure 1. a) Illustration of the three-step model of high-harmonic generation. After tunnel ionization, the continuum electron is accelerated by the laser field and recombines with the parent ion, resulting in the emission of an attosecond light burst in the extreme-ultraviolet part of the electromagnetic spectrum. b) Electron trajectories in an 800 nm laser field. The short trajectories corresponding to individual harmonic orders are defined by unique times of ionization and recombination. c) Corresponding HHG spectrum. Every emitted harmonic order can be associated with a unique transit time of the continuum electron. d), e) Same as (b) and (c) for 1300 nm.



aligned CO₂ molecules.^[63,79] These minima were attributed to the destructive interference of emissions from two centers of the molecules at a certain de Broglie wavelength of the returning photoelectron wave packet.^[80,81] Consequently, they were regarded as originating from the static electronic structure of the molecules. The importance of multielectron effects in interpreting these findings was described in Ref. [82]. These investigations used experimental data on CO₂ to benchmark theory and identified the multielectron dynamics by comparing experiment and theory. In a further pioneering experiment, the orbitals underlying the dynamics in N₂ were tomographically reconstructed.^[83] This approach again relied on the plane-wave approximation and sacrificed temporal resolution in favor of a tomographic reconstruction. All of these experiments paved the way towards measurements of electronic dynamics in molecules through HHS and are discussed in this Review.

1.3. Manifestations of Electron Correlation in Molecules in Time-Resolved Experiments

Much of the theoretical work on attosecond charge migration was motivated by the pioneering experiments by Weinkauff, Schlag, and co-workers,^[84,85] who observed selective bond dissociation after ionization of small peptides. These results raised the question of how a charge created by ionization can move across a molecule and eventually become localized at a particular site. A likely mechanism is that the charge oscillates across the molecule driven by purely electronic dynamics and is subsequently trapped through the coupling of the electron motion to the nuclear degrees of freedom.^[86–88] These purely electronic dynamics were called “charge migration” to distinguish them from the nuclear-dynamics-driven charge transfer.^[160] In particular, Cederbaum and co-workers subsequently showed that electron correlation can be a main driving force for charge migration.^[3,87]

Electron correlation imprints strong signatures on the electronic structure and dynamics of molecules. Neglecting large parts of electron correlations in molecules enables the description of a single electron in the mean-field of all other electrons, which is the central approximation of Hartree–Fock (HF) theory (electron correlation due to the exchange interaction of two electrons is already included in the HF theory; see for example, Ref. [1]). Thus, a stringent and broadly accepted definition of an energy attributed to electron correlation is the difference between the exact energy of a system and the energy obtained through a Hartree–Fock calculation in the limit of a complete basis set. Such quantities are however very difficult to measure, because experiments only provide access to energy differences.

The approximation of describing one electron in the mean field of all other electrons in Hartree–Fock theory is the direct consequence of approximating the true many-electron wavefunction by a single Slater determinant, which is an antisymmetrized product of one-electron wavefunctions, the so-called molecular orbitals. Molecular orbitals are one of the

most broadly applied and most successful concepts in chemistry. They are used for rationalizing chemical and physical properties of atoms and molecules as well as their reactivity.^[89] Furthermore, within Koopmans’ theorem, the energy of a single orbital is equal to the ionization energy to the final state of the cation. Within this framework, an electronic state of the cation is described as a one-hole configuration in the orbital under consideration.

The breakdown of the molecular-orbital picture as observed in X-ray photoelectron spectroscopy is therefore a direct consequence of strong electron correlation^[2] and can be observed experimentally through the appearance of satellite bands in the spectra. The appearance of these correlation-induced satellites is most prominent for inner-valence states, where the density of states is high and thus the electron-correlation effects are strong.

In time-resolved experiments using temporally confined ionization as a pump the signature of such strong correlations is a rapid quasi-exponential decay of the coherently prepared hole populations and all related observables due to the large number of prepared excited states.^[3] The situation is slightly more subtle in the outermost valence states, where the mixing of different configurations is less pronounced. Previous theoretical work^[3,5,87,88,90–92] has addressed the question of valence-shell charge migration in detail. This work typically assumes a sudden ionization process, which prepares a one-hole configuration in the neutral molecule. This hole can be approximated as one electron missing from a Hartree–Fock orbital of the neutral molecule as long as the neutral molecule is well-described by a single Slater determinant wavefunction. Depending on the extent of electron correlation of the cation, this one-hole configuration in the neutral molecule will correspond to a superposition of multiple electronic states in the cation and an oscillatory charge motion can be induced. On the contrary, if electron correlation is weak, the prepared state of the cation will be well described by a one-hole configuration in the neutral molecule and no dynamics will take place. Such a theoretical description enables the precise quantification of the contributions of electron correlation in the valence shell of molecules. However, experimental access to correlation-driven charge migration in the valence shell remains challenging because pulses with attosecond durations unavoidably have a broad spectral bandwidth and therefore populate multiple electronic states of the cation, independent of a possible strong mixing of these states owing to electron correlation.

Within the theoretical framework of correlation-driven valence-shell charge migration,^[3] the populations of the eigenstates will carry information about the extent of electron correlation. However, in a typical photoionization experiment, the ionization cross-sections determine the populations of the eigenstates of the cation, which encode electron correlation in a non-trivial way. The same is true for transient-absorption measurements, where the signal is related to absorption cross-sections. Thus, new experimental techniques and advanced methods of analysis are needed to directly decode correlation-driven electronic motion from experimental observables.

In this Review, we briefly outline the theoretical concepts of HHS and describe the capabilities of HHS to monitor electronic dynamics and charge migration in detail. We finally develop a theory which allows for the extraction of electron-correlation effects from the observables of HHS paired with accurate calculations of photoionization cross-sections and strong-field ionization rates. We also outline how new developments of HHS could provide experimental access to strongly correlated inner-valence phenomena.

2. Theory

2.1. The Classical Three-Step Model of HHG

The process of high-harmonic generation is commonly rationalized in the previously mentioned three-step model of HHG. Here, we briefly discuss the three-step model as well as its quantum-mechanical analogue, the Lewenstein model based on the strong-field approximation (SFA).^[93] The Lewenstein model provides grounds for more sophisticated analyses of the process of HHG.

Within the three-step model of HHG, the propagation of the electron through the continuum is described fully classically.^[46] Neglecting the Coulomb potential of the cation the continuum electron is accelerated by the force of the laser field acting on the electron, which is $d^2x/dt^2 = -F(t)$. All equations in this article are given in atomic units (a.u.) unless otherwise stated. Here, x is the position of the electron and $F(t)$ represents the amplitude of a linearly polarized laser field. To solve this differential equation, we introduce the boundary conditions that the electron appears in the continuum with no initial velocity ($dx(t')/dt = 0$) and no displacement from the cation ($x(t') = 0$). Here t' is the time of ionization. At the time of photorecombination, the displacement of the continuum electron from the cation has to be zero in addition ($x(t) = 0$). Introducing the vector potential as the time derivative of the electric field $F(t) = -\frac{\partial A}{\partial t}$, we obtain Equation (1):

$$\begin{aligned} x(t) &= \int_{t'}^t dt'' (A(t'') - A(t')) \\ &= 0 \quad (\text{condition for recombination}) \end{aligned} \quad (1)$$

Equation (1) fully defines the classically allowed electron trajectories that contribute to HHG. It supports classical calculations of the electron displacement during HHG. Furthermore, it can be utilized to calculate the mapping between ionization and recombination times by imposing $x(t) = 0$ and subsequently to calculate the associated kinetic energy gain of the continuum electron and thus the emitted photon energy upon recombination. Following this procedure, the relation

$$\Omega_{\max} = I_p + 3.17 U_p \quad (2)$$

for the maximum emitted photon energy Ω_{\max} , the so-called cutoff of the high-harmonic spectrum, is obtained. I_p is the ionization potential and $U_p = \frac{F_0^2}{4\omega_0^2}$ is the ponderomotive energy, which is the cycle-averaged kinetic energy of an

electron in a laser field. F_0 is the field amplitude and ω_0 is the angular frequency of the fundamental driving field. Equation (2) shows that obtaining higher photon energies by HHG is possible through employing long-wavelength driving lasers and/or higher intensities. The former suffers from the unfavorable reduction of HHG efficiency^[94] when increasing the wavelength, whereas the latter is inherently limited by ionization of the medium.

From the expression for the electron displacement $x(t)$ [Eq. (1)], the exact ionization and recombination times, which give rise to the emission of a given photon energy, can be derived. This procedure provides two unique solutions, the so-called long and short trajectories. The long trajectories ionize earlier and recombine later within the driving laser field, but give rise to the same emitted photon energies as the corresponding short trajectories. Experimentally, the contributions from different types of trajectories can be separated by proper phase-matching conditions.^[95] The classical model also supports even longer trajectories, which would correspond to an acceleration and deceleration of the continuum electron wave packet over multiple cycles in the laser field until the electron finally recombines. Such trajectories are however strongly suppressed, as the continuum electron wave packet spreads over time, which greatly reduces the recombination probability.

2.2. The Lewenstein Model of HHG

A quantum-mechanical formulation of the three-step model is the so-called Lewenstein model,^[93] which uses the strong-field approximation (SFA) to describe the ionized electron in the laser field. The main approximation of the Lewenstein model in particular and the SFA in general (the SFA is also applicable to other strong-field processes like strong-field ionization or laser-induced electron diffraction) is to completely neglect the influence of the Coulomb potential of the cation on the continuum electron, and to only consider the influence of the strong laser field on the electron. The propagation of the continuum electron by the laser field is described by plane waves. The Lewenstein model also includes the single-active-electron approximation, that is, it neglects the population of multiple states of the cation as well as laser-induced modifications of the electronic structure of the cation and the neutral species. Within the SFA an analytical expression for the wavefunction of the continuum electron can be derived, which can be subsequently used to compute the total emission dipole, which is responsible for HHG [Equation (3)]:

$$\mathbf{D}(t) = i \int_{t_0}^t dt' \int d\mathbf{p} \mathbf{d}_{\text{rec}}(\mathbf{p}, t) e^{-iS(\mathbf{p}, t, t')} \mathbf{d}_{\text{ion}}(\mathbf{p}, t'), \quad (3)$$

where $\mathbf{d}_{\text{rec}}(\mathbf{p}, t) = \langle \phi^0 | \mathbf{d}_k | [\mathbf{p} + \mathbf{A}(t)] \rangle$ is the photorecombination dipole matrix element (\mathbf{d} is the dipole operator and ϕ^0 is the orbital from which the electron is ionized), and $\mathbf{d}_{\text{ion}}(\mathbf{p}, t') = \langle [\mathbf{p} + \mathbf{A}(t')] V_L(t') \phi^0 \rangle$ is the strong-field ionization matrix element ($V_L(t) = \mathbf{d} \cdot \mathbf{F}_L(t)$ is the laser-molecule interaction term). The term $S(\mathbf{p}, t, t') = 0.5 \int_{t'}^t dt'' [|\mathbf{p} + \mathbf{A}(t'')|^2 + I_p(t - t')]$ in Equation (3) can be identified as the phase accumulated by

the electron in the continuum. The continua in the photo-recombination and strong-field ionization processes are both described with plane wave states $[\mathbf{p} + \mathbf{A}(t)]$ with kinematic momentum $\mathbf{k} = \mathbf{p} + \mathbf{A}(t)$. Importantly, the Lewenstein model recovers the three steps of the classical model: ionization, propagation, and recombination. Whereas ionization and recombination are described by the corresponding matrix elements, the propagation step is described by the phase term $S(\mathbf{p}, t, t')$, which corresponds to a semi-classical action, that is, the time integral of the kinetic energy of the electrons and the ionization potential of the cationic state it was ionized from. Equation (3) contains an integral over an infinite number of trajectories including all possible momenta and ionization/recombination times. However, only a few of these contribute significantly to HHS. As a consequence of the rapid variation of the semi-classical action as a function of its parameters, only the trajectories possessing a stationary semi-classical action are dominant. These trajectories can be determined by the saddle-point method,^[93] which reveals the existence of long and short trajectories with ionization and recombination times that are similar (but not identical) to the classical model.

As stated above, many approximations are made in the Lewenstein model. However, the model is rightfully celebrated owing to its simplicity and the correct description of the basic physics of the HHG process. Further developments to overcome the shortcomings are the inclusion of strong-field ionization to multiple states of the cation,^[82,96] the description of a dynamic population transfer between the states in the strong laser field,^[97] the presence of Stark shifts^[98,77] of the cation and laser-induced modifications of the electronic structure in general,^[99] and the inclusion of nuclear dynamics during HHG.^[48,49,100] Importantly, the Lewenstein model employs plane waves (or Volkov states) to describe the continuum states, which neglect the presence of the Coulomb potential. Using true scattering waves to describe the continuum greatly improves this approximation,^[54,68,69,70]

which is discussed in the next section. The other improvements that are required to turn the qualitative Lewenstein model into a quantitative theory for analyzing the observables of HHS of more complex molecules are discussed in this Review.

2.3. Scattering-Wave Description of the Photorecombination Process in HHG

In this section, we emphasize the importance of a correct description of the photorecombination process in HHG. This important improvement over the Lewenstein model is also contained in the very successful quantitative-rescattering theory,^[70] which expresses the high-harmonic spectrum as a product of the returning photoelectron wave packet and the photorecombination matrix elements.^[101–105] We illustrate this aspect using HHG spectra of Ar, which exhibit a deep minimum around 53 eV.^[69] Figure 2a shows the bound wavefunction of the outermost electron of argon and a two-dimensional cut through the continuum wavefunction, which was obtained from a scattering calculation. The oscillatory pattern of the continuum wavefunction is distorted in the vicinity of the ionic core owing to the presence of the ionic potential, which has a pronounced influence on the photorecombination dipole moment d_{rec} , the squared modulus of which is shown in Figure 2b. Since the continuum electron is ionized from a 3p orbital, the dominant partial waves in the total photorecombination dipole have s- and d-character. The total dipole moments obtained through the scattering calculation employing an effective core potential feature a deep minimum around 51 eV, which arises from a sign change in the dipole amplitude of the d-wave recombination. The minimum predicted through pure plane waves is found close to 21 eV, whereas Coulomb waves predict no minimum at all in the relevant energy range.

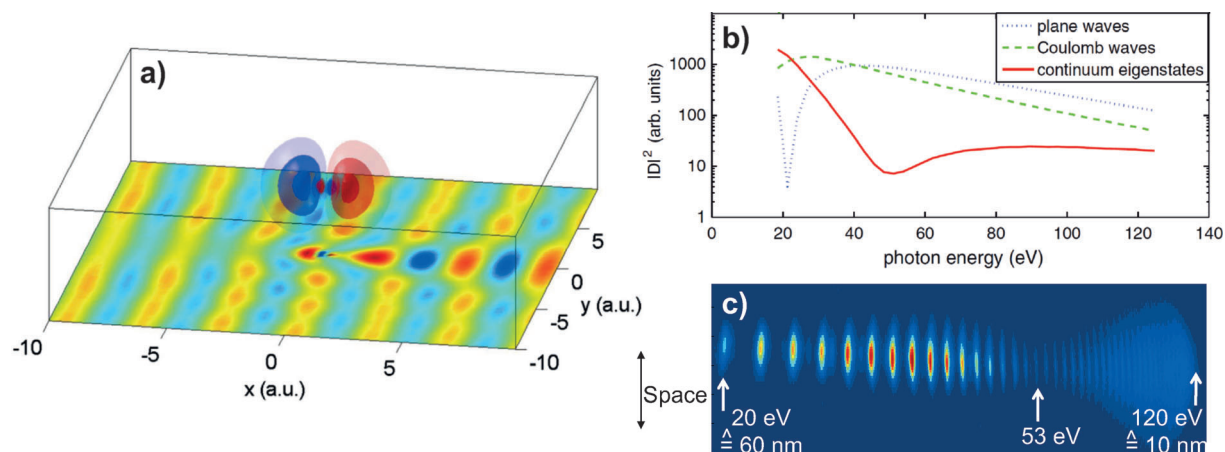


Figure 2. a) $3p_x$ ($m_l=0$) orbital wavefunction of argon and two-dimensional cut through the real part of the continuum wavefunction with partial-wave components from $\ell=0$ to $\ell=50$ for $k=1.8$ a.u. b) Square modulus of the recombination dipoles $|D|^2$ as a function of the photon energy for argon. The full line is the result obtained with scattering continuum wavefunctions, the dashed line was obtained from Coulomb wavefunctions, and the dotted line from plane wavefunctions. c) HHG spectrum from Argon generated with 40 fs, 1300 nm driving lasers. The position of the spectral minimum agrees well with the prediction of the recombination dipole by exact continuum functions. Parts (a) and (b) are taken from Ref. [69].

This minimum is indeed observed in the high-harmonic emission from Ar, as shown in Figure 2c, and was found at the same energy for different driving wavelengths, pulse durations and intensities.^[69,106] This clearly shows that the minimum arises from the electronic structure of the Ar atom and is encoded in the photorecombination dipole, which is independent of laser parameters such as intensity and wavelength of the driving pulses. Indeed, the spectral minimum in Ar has been studied with synchrotron light sources in detail and lies close to the minimum in the photoionization spectrum known as Cooper minimum.^[107] However, other examples of molecules such as CO₂, N₂O and ICCH feature minima in their HHG spectra, which are both intensity and wavelength dependent, and thus cannot be ascribed to originate from the electronic structure alone. The next sections will elucidate these findings.

3. Signatures of Electron Dynamics in High-Harmonic Spectra of Atoms and Aligned Molecules

3.1. Correlated Electron Dynamics in the Giant Resonance in Xenon

The findings in argon motivated the application of HHG to study electronic-structure phenomena, which were previously studied by synchrotron light sources. The recolliding continuum electron typically returns to the orbital it was

initially ionized from. The high-harmonic spectrum therefore contains information on the electronic structure of the ground state of the investigated system as illustrated in Figure 3a for HHG from xenon.

However, high-harmonic spectroscopy can also be used to investigate collective electronic dynamics, which is both induced and probed by the recolliding electron. As the kinetic energy of the recolliding electron is typically larger than the energy difference of electronic levels, the recollision can occur inelastically. Thus, the continuum electron can recombine to a different hole than the one left behind upon ionization, while simultaneously exciting another bound electron into the initially created hole, which is illustrated in Figure 3b. Such multi-electron dynamics induced by the continuum electron can be observed in xenon. Figure 3c shows the HHG spectrum of xenon obtained with sub-two cycle driving pulses centered at 1800 nm. The most striking feature is a pronounced peak around 100 eV. This maximum has been studied in detail in photoionization experiments and ascribed to the influence of 4d electrons on the cross section of the 5p electrons, because the 4d electrons have a large photoionization cross section due to a shape resonance in this energy region.^[108] Nevertheless, it comes as a surprise that the 4d electrons, which have a binding energy of 68 eV and thus a very low tunneling-ionization probability, participate in HHG. The reason is an inelastic HHG channel: Upon recollision, an energy exchange between the 4d electrons and the recolliding electron takes place. Thus, the continuum electron loses 56 eV of kinetic energy to promote electrons

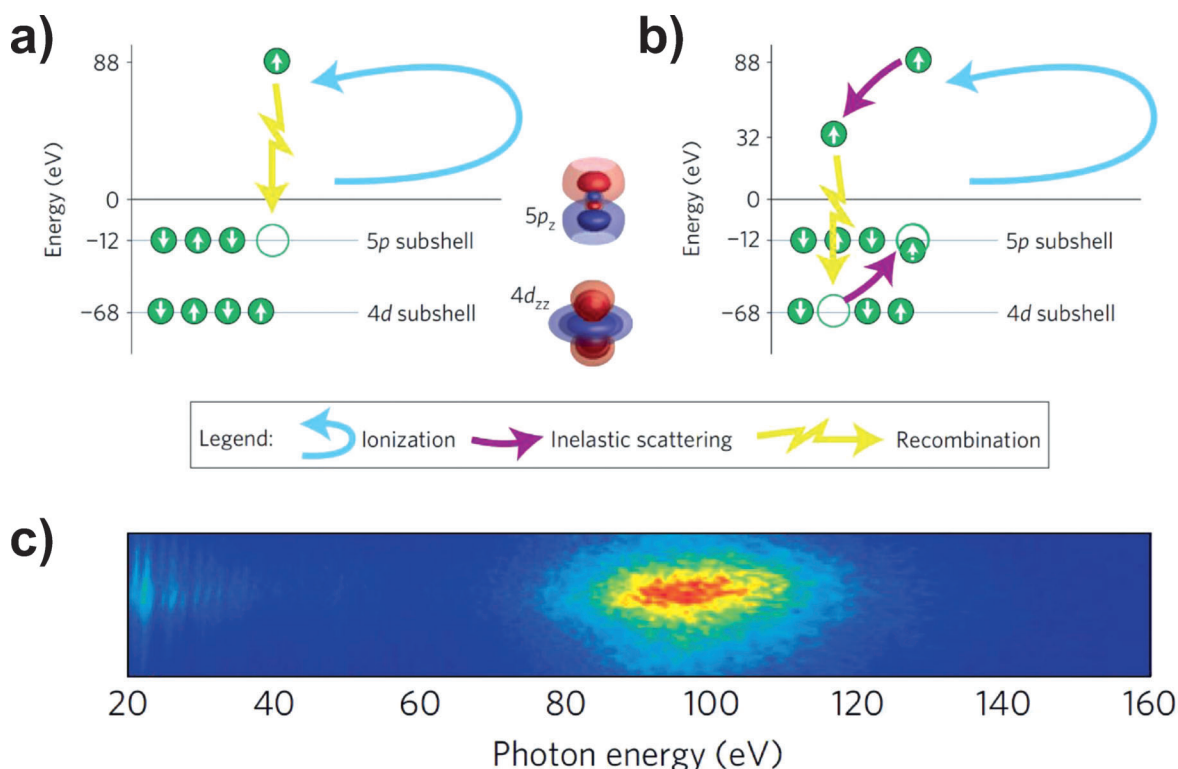


Figure 3. HHG enhancement at the giant dipole resonance in xenon. a) The three-step model suggests ionization from and recombination to the 5p orbitals. b) Owing to inelastic scattering, the returning electron can excite a lower-lying electron from a 4d orbital into the 5p vacancy and subsequently recombine to a 4d orbital, causing a giant enhancement of the HHG signal at 100 eV in xenon. c) Raw HHG spectrum from xenon generated with sub-two cycle pulses at a center frequency of 1800 nm and an intensity of 1.9×10^{14} Wcm⁻². Taken from Ref. [71].



from the 4d into the 5p subshell, and subsequently recombines into the 4d shell, where the harmonic emission is resonantly enhanced through the presence of the 4d shape resonance. Owing to the much higher binding energy of the 4d shell, the decelerated electron recombining to the 4d shell emits HHG at the same photon energy as that of the direct 5p channel. This giant resonance enhancement of HHG in Xe has been predicted and confirmed in theoretical studies.^[72,109]

The giant enhancement in xenon illustrates how HHG can be used to probe dynamic processes induced by electron correlations between the continuum and the bound electrons. We will now proceed to discuss how the signatures of bound multielectron dynamics in high-harmonic spectra can be identified.

3.2. High-Harmonic Spectroscopy of Multi-Electron Dynamics in Molecules

Generally, molecular cations have closer-lying electronic states than atoms. This enables the direct population of more than one electronic state of the cation through strong-field ionization, which are otherwise suppressed due to the exponential dependence of strong-field ionization on the ionization potential. In a molecular-orbital picture, this corresponds to ionization from different orbitals (HOMO, HOMO–1, HOMO–2). This representation is adequate as long as the electronic eigenstates are well described as single-hole configurations of the multi-electron wavefunction of the neutral molecule, which is a good approximation for the three lowest-lying electronic states of CO_2^+ .

The process of HHG from multiple molecular orbitals is illustrated in Figure 4a for the case of CO_2 aligned parallel to the polarization of the laser pulse. The parallel alignment of the molecule increases the ionization rate to the second excited state $\tilde{\text{B}}^+ 2\Sigma_u^+$ due to the σ_u symmetry of HOMO–2, such that the molecule is mainly ionized to the $\tilde{\text{X}}^+$ and $\tilde{\text{B}}^+$ states. Thus, HHG can be described as the coherent addition of the emissions from two different electronic states of the cation. These two channels carry electronic-structure information encoded in the photorecombination dipole moments and the alignment-dependent ionization rates. The phase of the emission from the second excited state $\tilde{\text{B}}^+$ relative to the emission from $\tilde{\text{X}}^+$ depends mainly on the difference of the transit times of the electron in the continuum. Since the emitted photon energy maps onto the electron transit time in a unique way, the relative phase of the two channels varies across the emitted photon energies, and can cause destructive (or constructive) interference.

Experimental data for HHG generated with 800 nm driving fields and different driving intensities for CO_2 molecules aligned parallel with respect to the polarization of the laser field are shown in Figure 4b. A clear minimum is present in the spectral envelopes, which shifts to higher harmonic orders with increasing driving intensities. The origin of this intensity-dependent minimum is a destructive interference between the $\tilde{\text{X}}^+$ and the $\tilde{\text{B}}^+$ HHG emission channels. The phase that is due to the electronic wave packet evolution, which is launched by strong-field ionization, amounts to $2.44 \pm 0.2\pi$ at the spectral minimum corresponding to a transit time of about 1.1 fs, and the phase difference in the photorecombination dipoles of the two channels is 0.5π , bringing the total phase to about 3π , which causes destructive

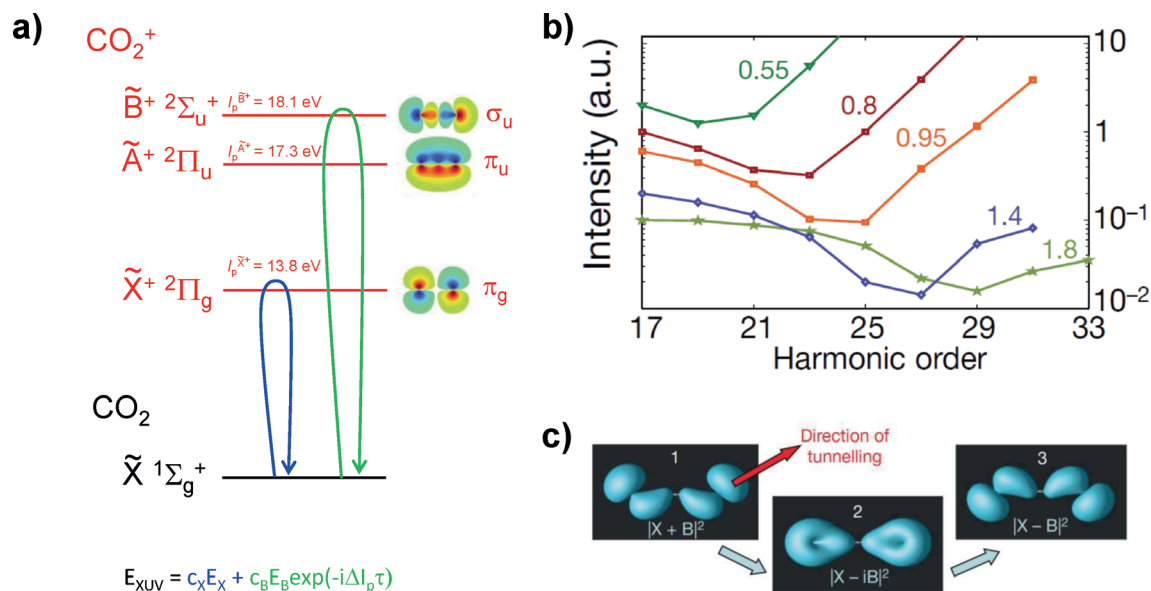


Figure 4. a) Multi-electron HHG in CO_2 . SFI of CO_2 molecules aligned parallel to the polarization of the laser field can prepare the cation in the $\tilde{\text{X}}^+ 2\Pi_g$ ground state (ionization from HOMO) and the $\tilde{\text{B}}^+ 2\Sigma_u^+$ second electronically state (ionization from HOMO–2), which contribute to HHG. The emitted HHG E_{XUV} can be described as an interference of HHG emissions from the $\tilde{\text{X}}^+ 2\Pi_g$ and the $\tilde{\text{B}}^+ 2\Sigma_u^+$ states. b) HHG intensity ratios (integrated over each harmonic order) between molecules aligned parallel ($\theta = 0^\circ$) and under $\theta = 50^\circ$ with respect to the polarization of the HHG driving laser pulse for different intensities (in units of $10^{14} \text{ W cm}^{-2}$). The spectra are shifted vertically for better visibility. c) Calculated electron hole density at 1) the instant of ionization, 2) after 240 as corresponding to a quarter period of the electronic wave packet, and 3) after 480 as corresponding to half a period of the electronic wave packet in CO_2^+ . Parts (b) and (c) are taken from Ref. [82].

interference. By varying the intensity, the mapping between harmonic order and transit time is changed, which causes the minimum to shift in energy. Figure 4c illustrates the wave packet motion in CO_2^+ underlying the dynamic minimum in the HHG spectra at three different times: the instant of ionization, the quarter period of the wave packet evolution (after 240 as), and half of the period of one wave packet oscillation (480 as). It is important to emphasize that these images are purely qualitative because they assume equal populations of the two electronic states of the cation, which does not correspond to the situation encountered in the experiment. They moreover contain no information derived from the experiment, except for the relative phase of the two states at ionization. As we argue in Section 5.2, the determination of this relative phase is subject to a fundamental limitation inherent to the considered case of CO_2 .

The situation becomes more involved when turning to longer-wavelength driving lasers to generate higher photon energies and access longer transit times. High-harmonics generated in CO_2 with a driving wavelength of 1.45 μm revealed an intensity-independent minimum,^[67] whereas other studies still found intensity dependent minima at 1.3 μm ^[55] and 1.2 μm .^[54] Systematic intensity and wavelength scalings were carried out in Refs. [110,111] to explain these surprising findings and the pertinent results are shown in Figure 5. Experimental spectra at (a) 1.17 μm and (b) 1.46 μm show intensity-dependent and intensity-independent minima, respectively.

This finding of an intensity-dependent minimum at shorter driving wavelengths and an intensity-independent minimum at longer wavelengths can be explained by the combined effects of multi-orbital HHG and structures in the photorecombination cross-section, which are included in the simulations shown in Figures 5c,d through quantum scattering calculations using ePolyscat,^[112,113] which fully reproduce the experimental observations. Figures 5e,f show the channel-resolved contributions from HOMO and HOMO–2 to the high-harmonic emission spectrum calculated for laser pulses with central wavelengths of 1.2 μm and 1.44 μm .

For a wavelength of 1.2 μm the intensity of the emission from HOMO–2 is comparable to that of HOMO in the

cutoff. This is no longer the case for a wavelength of 1.44 μm , where the contribution of the HOMO–2 remains small compared to the contribution from the HOMO over the complete spectral region, which makes the contribution from HOMO–2 too small for effectively interfering with the emission from the HOMO. From Figure 5f it is obvious that the minimum in the spectra recorded at 1.44 μm originates solely from the HOMO channel through a two-center interference.^[63,79,80,81,110,111] Intensity-dependent minima on the other hand arise when the HHG cutoff is close to this electronic-structure minimum from the HOMO, because the minimum enhances the relative contributions of lower-lying

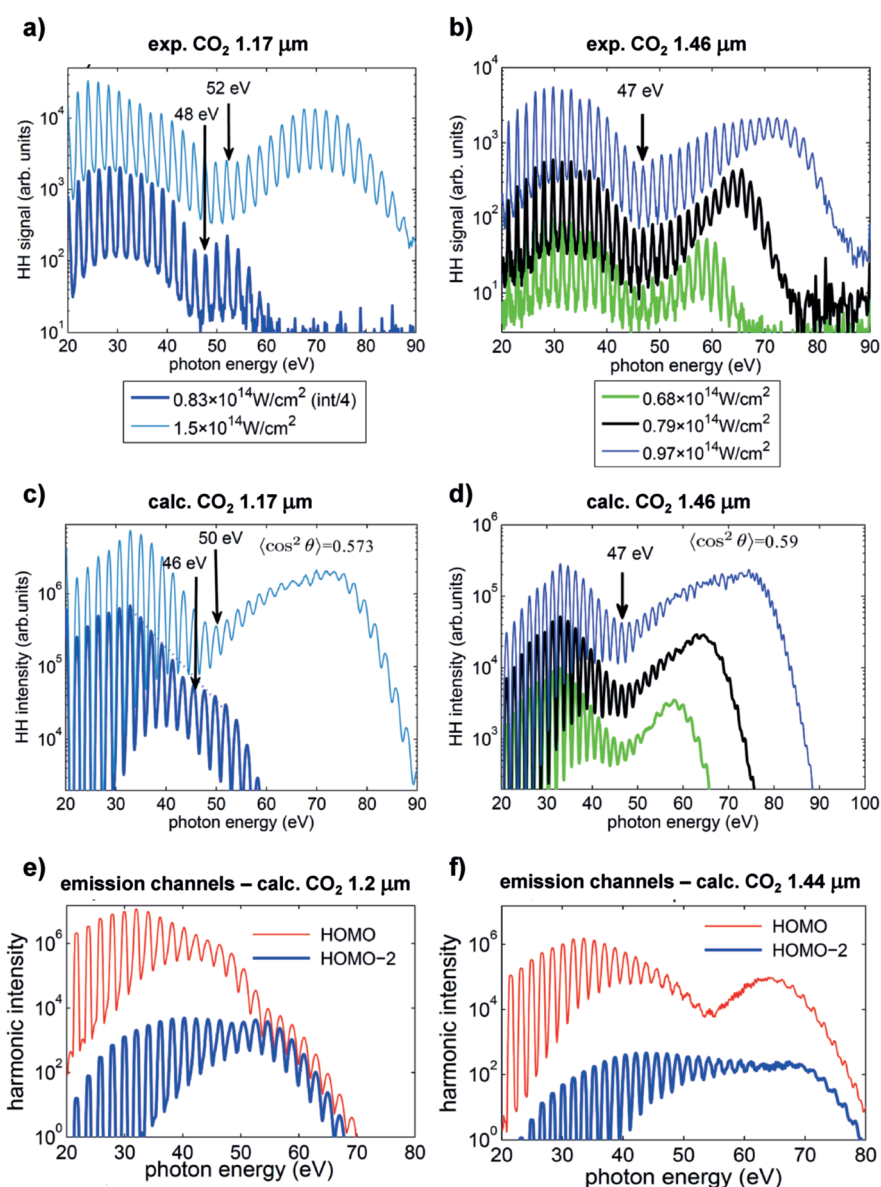


Figure 5. Experimental high-harmonic spectra generated in CO_2 molecules using 40 fs laser pulses for two different intensities centered at a) 1.17 μm and b) 1.46 μm . c),d) The corresponding calculated high-harmonic spectra. The degree of alignment is indicated. e),f) Calculated channel-resolved high-harmonic spectra for aligned CO_2 molecules ($\langle \cos^2 \theta \rangle = 0.5$), at a central wavelength of 1.2 μm and 1.44 μm , using a constant pulse length (40 fs) and intensity ($0.8 \times 10^{14} \text{ W cm}^{-2}$).



orbitals. This condition is generally fulfilled for wavelengths shorter than 1.4 μm in the case of CO_2 .

All of the work on CO_2 summarized in this section has described the electronic dynamics in the cation as quasi field-free, even though a strong laser field generating the high harmonics was present. This approximation was justified in the particular case of CO_2 molecules aligned parallel with respect to the polarization of the laser field, because the electric-dipole coupling between the $\tilde{X}^+ 2\Pi_g$ ground state and the $\tilde{B}^+ 2\Sigma_u^+$ second electronically state of CO_2^+ vanishes. More advanced theoretical modeling of HHG from CO_2 , including all laser-induced effects, was presented very recently.^[114] The possibility of laser-induced dynamics was first addressed^[97] through ellipticity measurements in N_2 . During HHG in N_2 , ionization can prepare the cation in the $\tilde{X}^+ 2\Sigma_g$ ground state and the $\tilde{A}^+ 2\Pi_u^+$ first electronically excited state, which can be strongly coupled by the laser field depending on the alignment angle of the molecules. However, the origin of the polarization properties of the HHG spectra of nitrogen molecules remains debatable, and could also be explained through purely structural effects contained in the photorecombination cross section of the electronic ground state of the nitrogen cation.^[75,115]

4. Reconstruction of Electron Dynamics from the Observables of High-Harmonic Spectroscopy

4.1. Quasi Field-Free Attosecond Charge Migration in Ionized Iodoacetylene

The preceding section provided guidelines on how to identify the signatures of electronic dynamics in high-

harmonic spectra. Ultimately the goal of HHS is to directly retrieve the field-free and laser-driven electronic dynamics from experimental data rather than only showing evidence for the dynamics through comparison with theory. First efforts to reconstruct the dynamics from experimental data of HHG from N_2 relied on amplitude and phase measurements of the emitted harmonics and employing a tomographic reconstruction procedure.^[83] While such an analysis enables the direct imaging of the dynamics, this approach degrades the temporal resolution to about 600 as in favor of the reconstruction procedure and requires the plane-wave approximation to describe the photorecombination process, which can fail as described previously in the case of the spectral minimum in argon (Figure 2).

In the following we describe how high-harmonic spectroscopy (HHS) has been further developed to reconstruct the full electronic quantum dynamics of charge migration in spatially-oriented polar molecules, which was introduced in Ref. [56]. The technique was applied to oriented iodoacetylene molecules and provided a time resolution of about 100 attoseconds. The reconstruction was applied to reconstruct quasi field-free charge migration as well as to demonstrate extensive laser control over the process. The reconstruction procedure generally relies on experimental results from several different measurements. The high-harmonic emission from oriented molecules was characterized in both amplitudes and phases at multiple wavelengths of the driving field.^[56] This set of experimental data enables the retrieval of the amplitudes and phases of the transiently occupied electronic states of the cation and the reconstruction of the initial shape of the hole created by SFI.

Iodoacetylene (ICCH) was chosen, because the two lowest-lying states of its cation can be appreciably populated

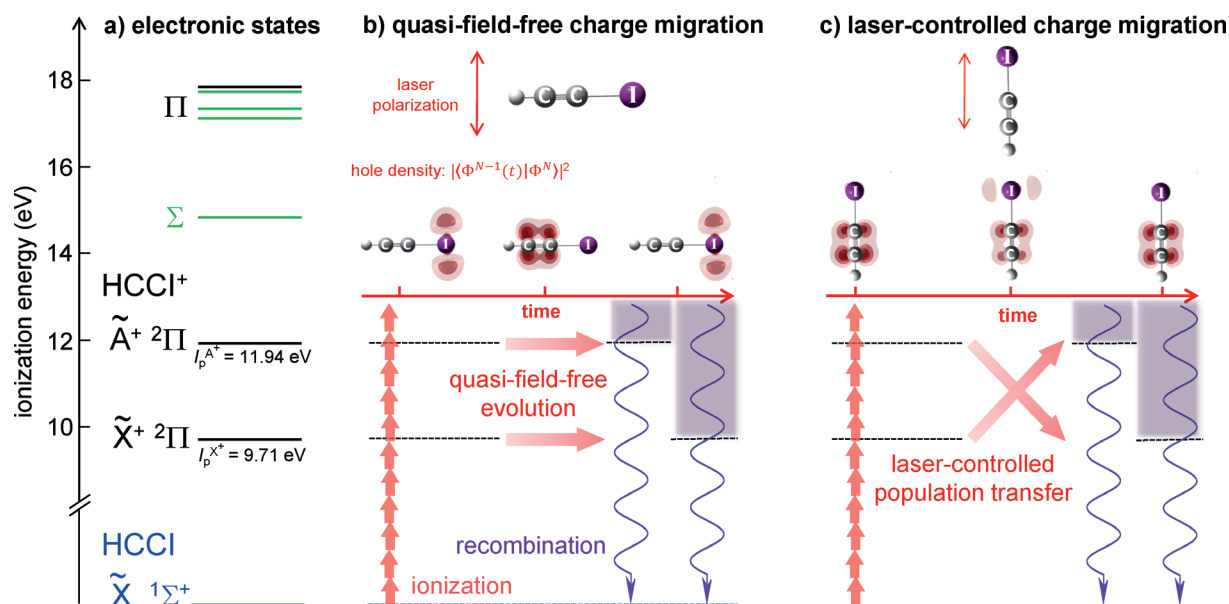


Figure 6. a) Electronic energy levels and conceptual scheme of b) quasi-field-free and c) laser-controlled charge migration in the iodoacetylene cation. An electron hole is created by strong-field ionization by infrared photons (red arrows). The temporal evolution of the hole density is encoded in the high-harmonic emission (violet arrows) at the instant of recombination. When the molecules are aligned perpendicular to the laser field as shown in (b), the populations of the \tilde{X}^+ and \tilde{A}^+ states are time-independent owing to the vanishing dipole coupling between these two states. Charge migration takes place as under field-free conditions. For parallel alignment strong population transfer between the \tilde{X}^+ and \tilde{A}^+ states is induced by the laser field, as depicted in (c). Taken from Ref. [56].

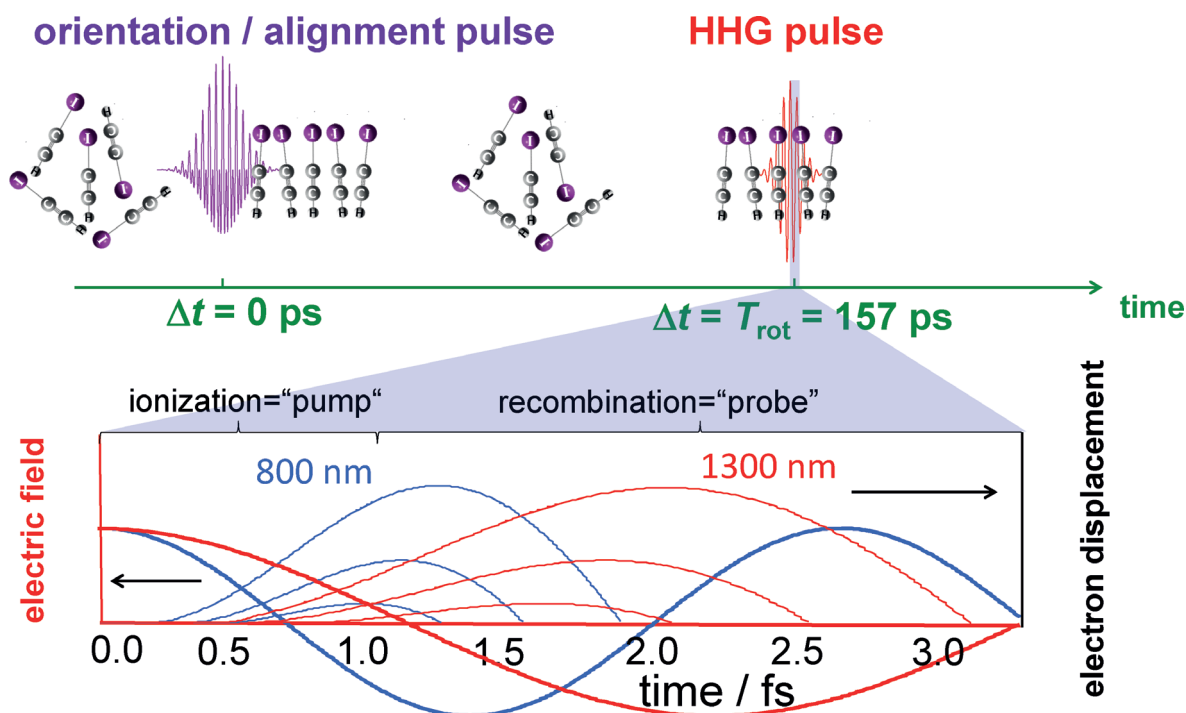


Figure 7. Concept of the experiment: The molecules are impulsively oriented using a two-color laser pulse. High harmonics are generated at the first full rotational period (upper panel). By selecting the short trajectories (thin lines, lower panel), a unique transit-time-to-energy mapping in the laser field (thick lines) is achieved. Changing the wavelength from 800 nm (blue) to 1300 nm (red) is equivalent to selecting a different time window of transit times for the continuum electrons.

by SFI. The two states possess hole densities that overlap significantly and therefore support pronounced charge migration from the iodine side of the molecular cation to the acetylene side. An energy-level diagram of ICCH^+ is shown in Figure 6. For molecules aligned perpendicular to the laser polarization (Figure 6b), the effect of the laser field on charge migration is negligible because the transition dipole moment between the two lowest electronic states of ICCH^+ is parallel to the principal molecular axis. We will discuss the quasi-field-free charge migration occurring for perpendicularly aligned molecules in this section. For parallel molecules (Figure 6c), the laser field transfers population between the \tilde{X}^+ and \tilde{A}^+ states and thereby controls charge migration, as discussed in the next section.

The concept of the experiment is presented in Figure 7. The molecules are impulsively oriented by an intense two-color laser field.^[116–118] The fixed-in-space ensemble of molecules is then interrogated by a HHG pulse one rotational period (157.0 ps) later under otherwise field-free conditions.

The reconstruction of charge migration in the cation requires multiple observables. High-harmonic intensity and phase measurements of aligned molecules with 800 nm and 1300 nm driving fields as well as high-harmonic intensity measurements of oriented molecules at 800 nm were performed.

Charge migration can be numerically reconstructed in terms of initial (as prepared by ionization at t') and final (at the instant of photorecombination, t) populations and phases of the states of the cation in a numerical inversion problem employing a generalized theory of HHG, which describes all

experimental intensity ratios and phase differences between molecules aligned parallel or perpendicular to the laser field. Following the Lewenstein model as discussed in Section 2.2,^[93] the high-harmonic emission dipole moment $\mathbf{D}(\mathbf{p}, t, t', \theta)$ can be generalized to include all effects relevant for polar molecules, and written as a function of electron momentum \mathbf{p} , the ionization and recombination times t' and t , and the orientation angle θ as in Equation (4):

$$\mathbf{D}(\mathbf{p}, t, t', \theta) \propto i \sum_{i,f} \int_{t_0}^t dt' \int d\mathbf{p} \mathbf{d}_{\text{rec},f}(\mathbf{p}, t, \theta) c_{if}(t, t', \theta) \cdot a_{\text{EWP},i}(\mathbf{p}, t, t') C_i(t, t') r_i(t') \mathbf{d}_{\text{ion},i}(\theta). \quad (4)$$

Applying the saddle-point method to Equation (4) leads to an expression of the dipole moment in the frequency domain $\mathbf{D}(\Omega, \theta)$. Based on this formulation, expressions for the phases and amplitudes of the emitted high harmonics can be derived. The angle-averaged initial populations $|r_i|^2$ as well as final populations $|c_{if}|^2$ and relative phases between these populations are retrieved in a global nonlinear least-squares optimization. Following the advances in HHS described in the previous sections of this Review, the theory underlying the reconstruction [Eq. (4)] includes all relevant electronic states i, f , the continuum structure through the use of scattering-wave matrix elements $\mathbf{d}_{\text{rec},f}$,^[70] nuclear motion through autocorrelation functions C_i derived from photoelectron spectra,^[100] the continuum electron wave packet $a_{\text{EWP},i}$ and the molecular axis distribution. The mapping from photon energy to transit time ($\tau = t - t'$) is performed using



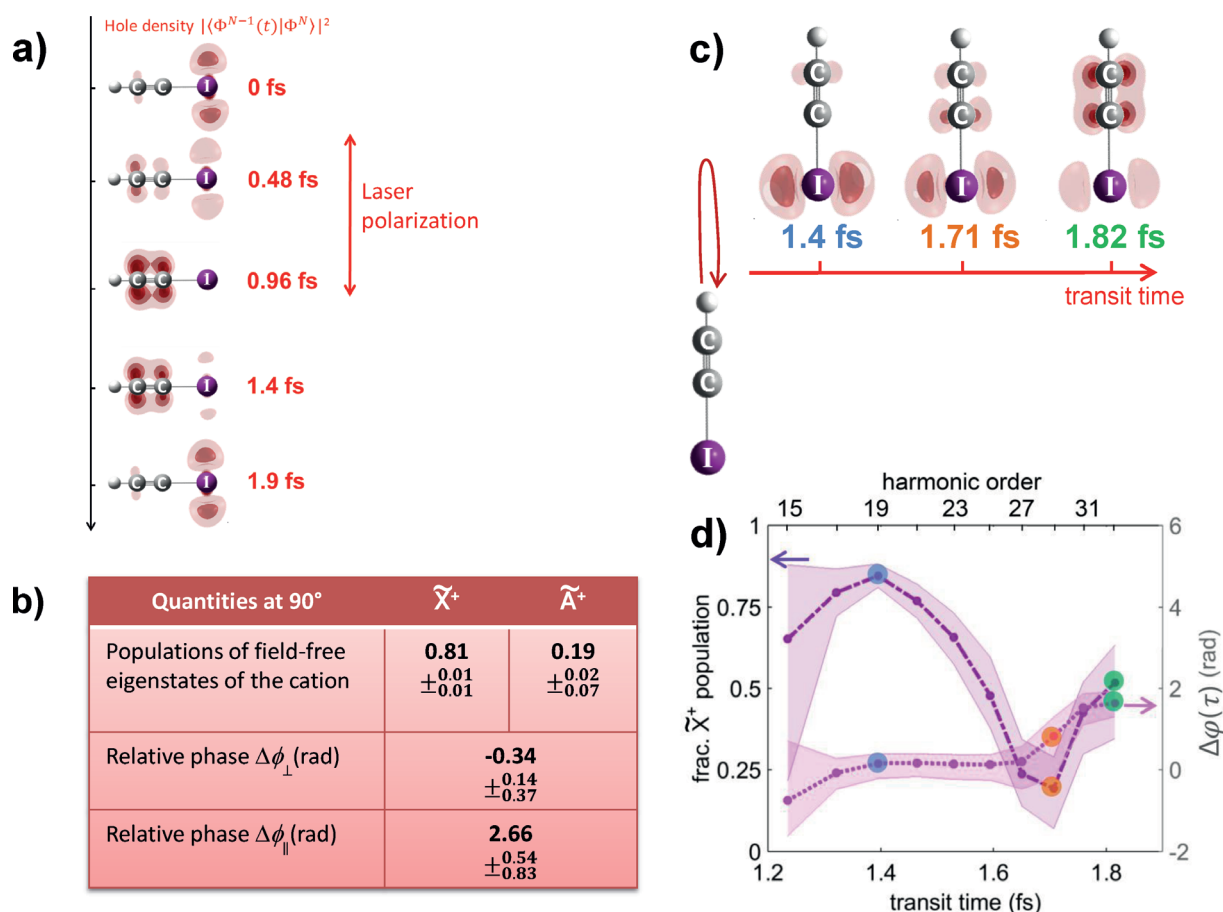


Figure 8. a) The reconstructed electron dynamics displayed as a function of time after ionization. Reconstructed values are given for b) the population amplitudes $|p_i|$ ($i = \tilde{X}^+, \tilde{A}^+$) for perpendicular alignment and the relative initial phase $\Delta\phi$. c) Reconstructed hole densities at selected transit times and d) reconstructed population of the \tilde{X}^+ state (dash-dotted violet line, the time-dependent population of the \tilde{A}^+ state is given by normalization) and relative phase between the \tilde{X}^+ and \tilde{A}^+ states (dashed magenta line) for a driving wavelength of 1300 nm and electron tunneling via the hydrogen atom.

quantum electron trajectories obtained by the saddle-point method.^[59,93,109]

The reconstruction of charge migration for molecules aligned perpendicular to the 800 nm driving field is shown in Figure 8a. The reconstructed initial populations (Figure 8b) were found to agree well with time-dependent density functional theory^[56,119] and with the weak-field asymptotic theory.^[120–124] Combined with the experimentally retrieved initial phase $\Delta\phi = \varphi_{\tilde{A}^+}(\tau=0) - \varphi_{\tilde{X}^+}(\tau=0)$ (Figure 8b) between the ground and first excited electronic states of the cation, charge migration is reconstructed as shown in Figure 8a. The spatial representation of the electron densities further requires the computation of molecular orbitals and the knowledge of the difference of the vertical ionization potentials of the field-free eigenstates, which determines the oscillation period of 1.85 fs and is known from photoelectron spectroscopy.^[125] Strong-field ionization is found to create a one-electron hole localized on the iodine side of the molecule, compatible with the low ionization potential and high polarizability of the iodine atom. Subsequently, the hole delocalizes over the molecule and then localizes at the acetylene side after 930 as.

Furthermore, a difference of about π in the relative initial phase of the \tilde{X}^+ and \tilde{A}^+ states for parallel alignment was reconstructed (Figure 8b)), which implies that the hole is created on the acetylene side. This means that the electron hole is created on the opposite side from where the electron tunneled because ionization via the iodine atom is dominant. The reconstructed hole is moreover consistent with ionization to the lowest-lying multi-electron eigenstate of the cation in a static electric field corresponding to the experimental laser peak intensity.

4.2. Laser control of charge migration

Strong laser control over charge migration can be exerted by a coupling between the laser field and the transition dipole moments of the cation prepared by SFI. A dipole moment is generally a vectorial quantity. Therefore, orienting the molecules provides a way to control the influence of the laser field on the induced dynamics. The extent of laser control over the dynamics is determined by the coupling strength between the target system and the laser field, which

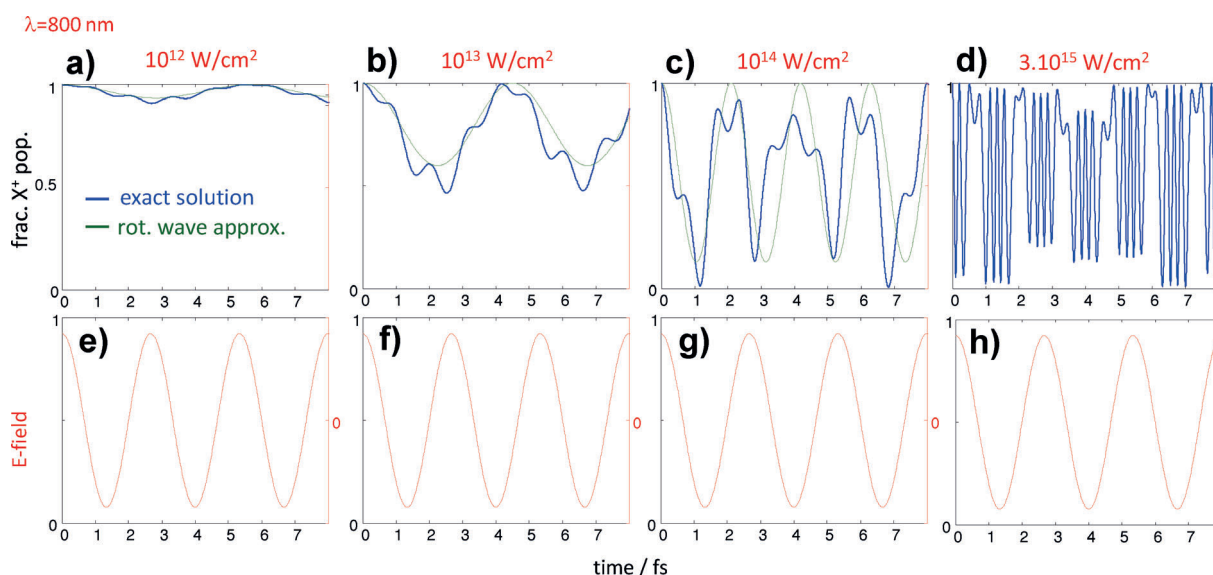


Figure 9. a)–d) Fractional population of the electronic ground state of ICCH^+ in a strong 800-nm laser field for parallel alignment, treated as a two-level system, for different intensities. The blue line shows the exact solution of the time-dependent Schrödinger equation, whereas the green line is the solution within the rotating-wave approximation neglecting higher-order frequencies in the population transfer. The laser field is depicted in the panels (e)–(h).

is given by the field strength, the detuning between the transition energies of the cation and the photon energy of the laser field and the magnitude of the transition dipole moment. Thus, changing the wavelength and the intensity of the driving fields allows extensive laser control over the laser-induced electron dynamics in the cation.

The ground and first excited states of ICCH^+ are coupled by a large transition dipole moment (1.35 atomic units, which is equivalent to 3.43 Debye) lying parallel to the molecular axis. Thus for parallel alignment the ionization-induced charge migration is controlled by the laser field (Figure 8c,d) and differs substantially from the field-free evolution (Figure 8a). In Ref. [56] the orientation-dependent charge migration was reconstructed for tunneling from the iodine as well as the acetylene side of the molecule using driving wavelengths of 800 nm and 1300 nm. The results for tunneling from the acetylene side and 1300 nm are shown in Figure 8c,d. Figure 8d shows the fractional population of the \tilde{X}^+ ground state (dash-dotted purple line) and the relative phase $\Delta\varphi(\tau) = \varphi_{\tilde{A}^+}(\tau) - \varphi_{\tilde{X}^+}(\tau)$ between the \tilde{X}^+ and \tilde{A}^+ states (dotted magenta line) for all reconstructed delays. Strong population transfer by the laser field is found. The fractional ground-state population gradually increases until 1.4 fs and then decreases again. The reconstruction shows a second minimum of the \tilde{X}^+ population at 1.7 fs and a subsequent rise for longer delays. The electron hole densities (Figure 8c) reconstructed from the populations and relative phases demonstrate the strong laser control over the dynamics.

We now discuss the origin of the laser control over the dynamics for parallel alignment in more detail. Figure 9 shows the fractional ground-state population of iodoacetylene treated as a two-level system for different intensities in a strong 800 nm laser field. The treatment of ICCH^+ as a two-level system was verified in Ref. [56] to be accurate by

comparison with 10-level calculations. For low intensities ($10^{12} \text{ W cm}^{-2}$, Figure 9a), the ground-state population is well described by Rabi oscillations. The blue line shows results that were obtained by solving the time-dependent Schrödinger equation (TDSE) for two levels. The green line represents the result obtained within the rotating-wave approximation and therefore oscillates exactly with the Rabi frequency. The Rabi frequency depends on the intensity of the driving field, the dipole-transition moment and the detuning of the central frequency of the laser pulses from the energy separation of the two levels. For higher intensities ($10^{13} \text{ W cm}^{-2}$ and $10^{14} \text{ W cm}^{-2}$, Figure 9b,c), higher frequencies become apparent in the exact solution of the TDSE (blue line), which are not captured by the rotating-wave approximation (green line). At $10^{14} \text{ W cm}^{-2}$, the Rabi frequency is very similar to the frequency of the driving laser field, which leads to a dephasing of the periodicity of the population transfer as compared to the solution within the rotating-wave approximation for later times (see for example, around 6–7 fs for $10^{14} \text{ W cm}^{-2}$, Figure 9c). This intensity is essentially the same as that applied in the experiments presented in this section. The strong laser control over the dynamics is thus a consequence of the very intense field, combined with a large transition-dipole moment. The resulting electronic dynamics is highly non adiabatic, that is, the Rabi frequency is similar to the laser frequency, which leads to large deviations of the exact solution from the rotating-wave approximation and the appearance of additional frequencies in the population dynamics. For even higher intensities ($3 \times 10^{15} \text{ W cm}^{-2}$, Figure 9d) the Rabi frequency is much higher than that of the driving field and thus responsible for the high-frequency modulations in the fractional ground-state population present in Figure 9d, a regime designated as carrier-wave Rabi flopping.



5. Perspectives for Decoding Electron Correlation by High-Harmonic Spectroscopy

5.1. Analysis of Correlation-Induced Dynamics in High Harmonic Spectra

Correlation-driven charge migration has been extensively discussed.^[3,5,87,90,91] Here we discuss how electron correlation can be theoretically treated and propose a new pathway how it could possibly be experimentally identified through HHS. In the case of configurationally mixed states, a both computationally and conceptually convenient basis for the field-free eigenstates of the cation $|\Phi^{N-1}\rangle$ is an expansion in hole configurations of the neutral molecule. We use such expansions both for the electronic states of the cation initially populated through strong-field ionization [Equation (5)]:

$$|\Phi_i^{N-1}\rangle = \sum_m \beta_{i,m}^{1h} |\Phi_m^{1h}\rangle + \sum_n \beta_{i,n}^{2h1p} |\Phi_n^{2h1p}\rangle + \dots \quad (5)$$

and the final states [Equation (6)]:

$$|\Phi_f^{N-1}\rangle = \sum_k \beta_{f,k}^{1h} |\Phi_k^{1h}\rangle + \sum_l \beta_{f,l}^{2h1p} |\Phi_l^{2h1p}\rangle + \dots \quad (6)$$

Inserting these expansions into the generalized expression for high-harmonic emission [Eq. (4)] gives Equation (7):

$$\mathbf{D}(\Omega, \theta) \propto \sum_{i,j,k,m} \beta_{f,k}^{1h} \beta_{i,m}^{1h} a_{\text{EWP},i}(\Omega) r_{i,m} \mathbf{d}_{\text{ion},m}(\theta) c_{if}(\Omega, \theta) \mathbf{d}_{\text{rec},k}(\Omega, \theta) \quad (7)$$

where in comparison to Equation (4) the coefficients $\beta_{f,k}^{1h}$ and $\beta_{i,m}^{1h}$ appear, which indicate the weight of all single-hole configurations appearing in the description of the states of the cation and are therefore representative of the degree of electron correlation. In Equation (7) only the coefficients of one-hole configurations appear, because any higher-order excitations (for example, 2h1p configurations) will usually have small ionization and recombination matrix elements. More generally, any matrix element of a one-electron operator (such as the dipole operator) is zero if the initial and final state wavefunctions are Slater determinants that differ by the occupation of more than one orbital.^[1]

We now discuss how Equation (7) can be interpreted physically. To keep the discussion transparent, we assume that strong-field ionization prepares the cation in a superposition of the ground and first excited state, both of which shall be formally described as a linear combination of single holes in HOMO (H0) and HOMO–1 (H1) of the neutral molecule. This situation resembles the case of two-hole mixing within the theoretical framework of charge migration.^[3,5] Therefore photorecombination can also occur to both one-hole configurations. The same is true for ionization to the ground and first excited state of the cation. This contrasts with the situation encountered in the simpler molecules (CO_2 and N_2) previously investigated by HHS. Configuration interaction thus gives rise to four channels that emit interfering XUV radiation, as illustrated in Figure 10. The relative weights of the channels are then determined by the relative strong-field-ionization amplitudes to the eigenstates of the cation as well

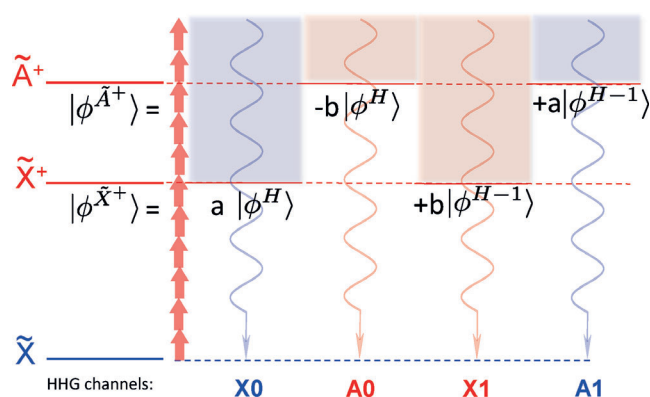


Figure 10. Charge migration driven by electron correlation: Configuration interaction introduces cross-channels into a HHG process formulated in a single-particle basis. Ionization and recombination can therefore connect different single-hole configurations. This gives rise to four emission channels if two states of the cation are coherently populated by strong-field ionization.

as the coefficients $a = \beta_{\tilde{X}^+, H0}^{1h} = \beta_{\tilde{X}^+, H1}^{1h}$ and $b = \beta_{\tilde{X}^+, H1}^{1h} = -\beta_{\tilde{X}^+, H0}^{1h}$. Ionization to \tilde{A}^+ followed by recombination to the HOMO hole is designated as channel A0, whereas ionization to \tilde{X}^+ and recombination to the HOMO–1 hole is channel X1. Different cationic states are connected to the same one-hole configurations via the photorecombination step owing to these correlation-induced cross-channels (X1 and A0). Their experimental identification would therefore provide the key evidence for correlation-driven charge migration.

A possibly very sensitive quantity to identify the importance of these correlation-induced HHG channels is the angle dependence of the harmonic emission dipole, that is, the angle dependence of the phase, amplitude, and polarization of the emitted radiation. These quantities can be measured through two-source interferometry,^[56,82,126] transient-grating spectroscopy^[75] and high-harmonic ellipsometry,^[127,128] respectively. Both photorecombination and strong-field ionization matrix elements are strongly angle-dependent quantities, and the correlation-induced cross-channels will have their own characteristic angle dependence. A comparison between a theory based on Equation (7) and angle-resolved measurements of high-harmonic intensity, phase and polarization can thus provide new information about electron correlation in molecules. Further techniques to continuously advance HHS are discussed in the outlook (Section 6).

5.2. Electron-ion entanglement

Both the degree of entanglement between the electron and ion and the electronic coherence between the electronic states of the cation are crucial quantities when hole dynamics are determined from high-harmonic measurements. Nevertheless, these aspects have been largely neglected to date. We first study the role of electron-ion entanglement and then turn to the role of the electronic coherence.

We consider the N -electron wavefunction $\Psi^N(t)$ of a molecule following strong-field ionization. The system is

generally in an entangled state, involving for example the two lowest electronic states of the cation [Equation (8)]:

$$\Psi^N(t) = \hat{A}[\Psi_{\tilde{X}^+}^{N-1}(t)\chi_{\tilde{X}^+}(t) + \Psi_{\tilde{A}^+}^{N-1}(t)\chi_{\tilde{A}^+}(t)] \quad (8)$$

where $\Psi_{\tilde{X}^+/\tilde{A}^+}^{N-1}(t)$ represents the electronic state of the cation in the laser field (contrary to $\Phi_{\tilde{X}^+/\tilde{A}^+}^{N-1}$, which represent the field-free states) and $\chi_{\tilde{X}^+/\tilde{A}^+}(t)$ the associated single-electron continua. Photorecombination from this state back to the initial electronic state of the neutral molecule is responsible for high-harmonic emission. A convenient basis for the single-electron continua is a partial-wave expansion, which we used previously to analyze the photorecombination step in carbon monoxide.^[78,77] Typically, only a few partial waves with different angular momenta have a major contribution to the total recombination matrix element owing to symmetry. As an example, photorecombination to a pure atomic p-orbital will exclusively take place from a continuum described by s- and d-waves (referring to angular momenta of $\ell = 0$ and $\ell = 2$), as in the case of HHG in argon (Ref. [69] and Section 3 of this Review).

Any statement about properties of the $N-1$ -electron wavefunction of the cation $\Psi^{N-1}(t)$, or equivalently, the one-electron hole defined as $\phi(t) = \langle \Psi^N | \Psi^{N-1}(t) \rangle$, is only possible if the wavefunction described by Equation (8) can be brought into a product form. This is generally not the case, as can be seen by rewriting Equation (8) to give Equation (9):

$$\Psi^N(t) = \hat{A}[c_{\tilde{X}^+}(t)\Psi_{\tilde{X}^+}^{N-1}(t) + c_{\tilde{A}^+}(t)\Psi_{\tilde{A}^+}^{N-1}(t)]\chi_1(t) + \hat{A}[c_{\tilde{X}^+}(t)\Psi_{\tilde{X}^+}^{N-1}(t) - c_{\tilde{A}^+}(t)\Psi_{\tilde{A}^+}^{N-1}(t)]\chi_2(t) \quad (9)$$

where [Equations (10) and (11)]

$$\chi_1(t) = \frac{\chi_{\tilde{X}^+}(t) + \chi_{\tilde{A}^+}(t)}{2} \quad (10)$$

$$\chi_2(t) = \frac{\chi_{\tilde{X}^+}(t) - \chi_{\tilde{A}^+}(t)}{2} \quad (11)$$

The degree of electron-hole entanglement is defined by the extent of overlap between the electronic continua $\langle \chi_{\tilde{X}^+} | \chi_{\tilde{A}^+} \rangle$, as can be readily seen from the norms of the wavefunctions given by Equation (10) and (11) [Equations (12) and (13)]:

$$\|\chi_1\|^2 = \frac{1 + \Re\langle \chi_{\tilde{X}^+}(t) | \chi_{\tilde{A}^+}(t) \rangle}{2} \quad (12)$$

$$\|\chi_2\|^2 = \frac{1 - \Re\langle \chi_{\tilde{X}^+}(t) | \chi_{\tilde{A}^+}(t) \rangle}{2} \quad (13)$$

A zero-overlap of the continua results in equal norms $\|\chi_1\|^2 = \|\chi_2\|^2 = 0.5$, that is, maximal entanglement owing to the fact that Equation (9) cannot be written in the form of a single product. As a consequence the two states of the ion inside the square brackets in Equation (9), which are orthogonal by construction, have the same probability amplitude, which means that the hole dynamics is completely undetermined.

Previous studies of electron-hole dynamics have concentrated on CO_2 ^[54,82,110,111] and N_2 ^[83] It turns out that in all of these studies, the ionization continua display exact orthogonality

imposed by their symmetry. The electronic continua contributing non-zero amplitudes to the harmonic emission dipole moment are of σ_u , π_u , and δ_u symmetry for the $\tilde{X}^{+2}\Pi_g$ state (one electron removed from HOMO) of CO_2^+ and of σ_g and π_g symmetry for the $\tilde{B}^{+2}\Sigma_u$ state (one electron removed from HOMO-2). In N_2 , the continuum symmetries contributing to the photorecombination dipole are σ_u and π_u for HOMO and σ_g , π_g , and δ_g symmetry for HOMO-1. Consequently, the corresponding overlap integrals $\langle \chi_{\tilde{X}^+} | \chi_{\tilde{A}^+} \rangle$ in the case of CO_2^+ and $\langle \chi_{\tilde{X}^+} | \chi_{\tilde{A}^+} \rangle$ in the case of N_2^+ are zero by symmetry. We note that this argument still holds for molecules that are aligned neither parallel nor perpendicular to the driving laser field. In this case the projection λ of the angular momentum of the continuum electron on the internuclear axis is no longer a good quantum number. However, inversion symmetry is still preserved over the entire HHG process, such that the gerade/ungerade symmetries of the involved continua result in zero overlap. This results in perfect ion-electron entanglement and therefore no information about the hole dynamics in the cation.

In the absence of such symmetry restrictions and especially in the case of configurationally mixed states, the situation is markedly different. Even without laser-induced dynamics between the electronic states, the continua associated with different electronic eigenstates of the cation overlap. This can be seen explicitly by converting the dipole moment in Equation (7) into the frequency domain and expanding it for two electronic states under the assumption that laser-induced dynamics are absent [Equation (14)]:

$$\begin{aligned} \mathbf{D}_\perp(\Omega, \theta) &\propto \sum_{i=(\tilde{X}^+, \tilde{A}^+); k=(1,2)} \beta_{f,k}^{\text{lh}} r_i a_{\text{EWP},i}(\Omega) \mathbf{d}_{\text{ion},i}(\theta) \mathbf{d}_{\text{rec},k}(\Omega, \theta) \\ &= [r_{\tilde{X}^+} \mathbf{d}_{\text{ion},\tilde{X}^+} a_{\text{EWP},\tilde{X}^+}(\Omega) (a \mathbf{d}_{\text{rec,HOMO}}(\Omega, \theta) + b \mathbf{d}_{\text{rec,HOMO}-1}(\Omega, \theta)) \\ &\quad + r_{\tilde{A}^+} \mathbf{d}_{\text{ion},\tilde{A}^+} a_{\text{EWP},\tilde{A}^+}(\Omega) (-b \mathbf{d}_{\text{rec,HOMO}}(\Omega, \theta) + a \mathbf{d}_{\text{rec,HOMO}-1}(\Omega, \theta))] \end{aligned} \quad (14)$$

which is the equation underlying Figure 10. Ionization to the ground state of the cation prepares one-hole configurations in the HOMO and HOMO-1 of the neutral molecule and so does ionization to the first excited state. It is thus also obvious that the ground and first excited state of the cation have overlapping continua as they are described by the same photorecombination dipoles ($\mathbf{d}_{\text{rec,HOMO}}(\Omega, \theta)$ and $\mathbf{d}_{\text{rec,HOMO}-1}(\Omega, \theta)$) weighted by different coefficients (a and b). The overlap integral $\langle \chi_{\tilde{X}^+} | \chi_{\tilde{A}^+} \rangle$ is thus nonzero, implying that a statement can be made about the electron-hole wavefunction and its time evolution. This non-zero overlap ultimately occurs if the electronic states of the cation share the same electronic symmetry and thus the same hole configurations contribute to their wavefunctions. Therefore, in the case of ICCH^+ , even though the lowest two electronic states do not display significant hole mixing, a statement about the electron-hole wavefunction and its time evolution can be made because the two electronic states share the same symmetry.

Equation (14) assumes that the photorecombination dipoles to the final states f of the cation $\mathbf{d}_{\text{rec},f}$ can be expressed as linear combinations of dipole moments representing one-hole configurations of the cation as a consequence of the



expansion of the final-state wavefunction Φ_f^{N-1} of the cation in Equation (6). This is true for recombination dipoles of the form $\mathbf{d}_{\text{rec},f}(\Omega, t) = \langle \Phi^N | \mathbf{D}^N | \Phi_f^{N-1} [\mathbf{p} + \mathbf{A}(t)] \rangle$ (where \mathbf{D}^N is the N -electron dipole operator), where the continuum wavefunction is represented by Volkov states, which have the mathematical form of a plane-wavefunction. If the effect of the Coulomb potential on the continuum states is explicitly taken into account, the expansion of $\mathbf{d}_{\text{rec},f}$ into matrix elements corresponding to one-hole configurations may be more involved. This aspect requires further investigation by multi-configurational electron-molecule scattering calculations.

5.3. Electronic Coherence

The second aspect that is critical for reconstructing hole dynamics in cations from high-harmonic spectroscopy is the mutual coherence of the electronic states of the cation. All previous publications (for example, Refs. [82,83]) have always assumed maximal coherence between the electronic states. However, both calculations^[129] and experiments^[36,130] have shown that strong-field ionization of even simple atoms does not result in maximal coherence between the electronic states of the cation. A simple general model for evaluating the degree of coherence of electronic states prepared by SFI has been given in Ref. [131]. This work showed that the coherence between ionic states prepared by SFI is mainly limited by the temporal confinement of the ionization step. Hence the crucial question arises: Is high-harmonic spectroscopy sensitive to the mutual electronic coherence of electronic states and to what extent?

In the case of orthogonal continua ($\langle \chi_{X^+} | \chi_{A^+} \rangle = 0$), Equation (8) leaves the relative phase of the cationic eigenstates undefined. This is seen from Eq. (9), where both the in-phase and out-of-phase combinations of the two electronic states are weighted by identical continuum norms. What about the case of configurationally mixed states?

In the case of configurationally mixed states a new situation arises. As illustrated in Figure 10 and Equation (14), configuration interaction gives rise to a total of 4 channels within a single-particle formulation of high-harmonic generation. Two channels correspond to the traditional situation that ionization and recombination occur from/to the same one-electron orbital representing the initial neutral state of the molecule. These channels are labeled X0 and A1 in Figure 10, representing the fact that strong-field ionization occurs to the electronic eigenstate \tilde{X}^+ followed by recombination to HOMO or ionization to \tilde{A}^+ followed by recombination to HOMO-1, respectively. Hole mixing between the cationic states opens two additional channels that are inactive in the absence of configuration interaction. These channels are labeled X1 and A0. They enable that ionization to the ground state of the cation can be followed by recombination to a HOMO-1 hole configuration and ionization to the first excited state can lead to recombination to a HOMO hole configuration. Thus their presence is an indication that two electronic states of the cation have overlapping continua. Consequently, these channels are sensitive to the mutual coherence between the cationic eigenstates.

6. Conclusions and Outlook

The past ten years have seen fundamental progress in applying the process of HHG as a spectroscopic technique for probing electronic structure and dynamics. In this Review, we highlighted the breakthroughs of both aspects of HHS, which offer new opportunities for probing electron-correlation induced dynamics in molecules. First, HHS is uniquely sensitive to the electronic structure of the target system used for HHG through the photorecombination dipole, as demonstrated for the electronic structure minimum in argon.^[69] Similar electronic structure effects have been investigated and demonstrated for molecular Cooper minima^[73,74,76] and shape resonances.^[73,75-78] Second, the unique mapping between electron trajectories and emitted frequencies serves as a tool for self-probing of molecular dynamics. First demonstrated for monitoring vibrational dynamics in H_2^+ , this idea was extended to study the interference of high harmonics emitted from different cationic states in CO_2 ^[82,110,111] and N_2 .^[83,97] Bringing these unique two features of HHS together, namely the sensitivity to both electronic structure and dynamics, required the development of a multidimensional measurement approach.^[56] The approach relied on measuring the amplitudes and phases of both aligned and oriented iodoacetylene molecules at multiple wavelengths and intensities. The experimental data were analyzed in the framework of a generalized theory, which enabled the retrieval of the attosecond dynamics in the molecular cation in terms of the populated field-free eigenstates. Furthermore, control over the alignment of the molecule in the strong laser field exerted extensive control over the attosecond electronic charge migration. This multidimensional measurement, which relied on measuring amplitudes and phases in Ref. [56], can be extended to more observables. This would allow the reconstruction of even more complex dynamics than those presented in Ref. [56], and in particular enable the reconstruction of correlation-driven electron dynamics as outlined by the theoretical analysis in this Review.

A few directions for new multidimensional measurements shall be discussed here. Polarization measurements such as ellipsometry can reveal subtle features of laser-driven electron dynamics as well as strong perpendicular components of emission dipole moments^[115] and thus generally serve as another observable in a multidimensional measurement approach. Attosecond lighthouse experiments^[132-138] with oriented molecules could give direct access to amplitude and phase asymmetries for the different recollision sides of oriented molecules. Two-color HHG experiments^[58-60,139-142] in combination with molecular orientation^[77,78,99,116-118] can provide a new observable for the reconstruction. The polarization of the second color can be chosen to be perpendicular to that of the first color to solely manipulate the electron trajectories^[59,140] and not the tunneling process. In combination with orientation, such experiments could reveal the side-specific amplitude and phase asymmetries of the HHG emission. Further options to employ shaped electron trajectories for self-probing of the evolving electronic structure are counter-rotating circularly polarized two-color fields. So far,



such fields have mainly been employed to generate circularly polarized harmonics.^[143,144] Recently, high-harmonic spectroscopy based on bicircular driving fields has been introduced^[145] and been shown to be a powerful probe of static and dynamical electronic symmetries of atoms and molecules.^[161]

Finally, the phase measurements in Ref. [56] employed the interference of two separate high-harmonic sources. Other phase measurements, which characterize the spectral phase rather than the angle-dependent phases are RABBIT measurements,^[17,83,146,147] streaking experiments,^[18,148–152] and HHG experiments with mixed gases,^[153] which have recently been combined with two-source measurements to access alignment-angle-resolved and energy-resolved phase information.^[154]

A promising extension of HHS for probing attosecond correlation-driven electron dynamics is XUV-initiated high-harmonic generation,^[155,156] where an XUV pulse is superimposed with an IR driving field. The XUV pulse initiates HHG by single-photon ionization, and the overlapped IR pulse accelerates the electron and drives it to recombination. This technique has the advantage that inner-valence states can be ionized, which typically exhibit strong electron correlation. The methods described in this Review can directly be generalized to XUV-initiated HHG, such that the strongly correlated dynamics following XUV ionization can be reconstructed from the spectra. XUV-initiated high-harmonic generation can access a very broad range of states owing to the short pulse durations and large bandwidths of attosecond XUV pulses. This might enable the study of the fastest collective electronic responses within the first tens of attoseconds following ionization.^[157] The only other technique that currently provides the necessary time resolution for such an experiment is attosecond streaking, which was indeed very recently successfully applied in measuring the energy-dependent phases in atomic photoionization and the associated delays of shake-up excitation in helium.^[158]

Following electron dynamics by HHS is an advanced form of spectroscopy that requires a thorough theoretical understanding of the HHG process and a reconstruction based on advanced theory. However, it bears several unique features compared to other techniques. Photofragmentation techniques are well suited for following dynamics of molecules, but the interpretation of the fragment yields requires a detailed knowledge of all potential energy surfaces.^[31] Transient-absorption spectroscopy can in principle follow both amplitudes and phases of the involved eigenstates,^[36] but the observed experimental quantities cannot easily be related to the characteristic configuration mixing coefficient in strongly correlated systems. Thus multidimensional HHS, involving a multitude of experimental observables, provides a promising route to capturing the complex and fascinating phenomena of correlation-driven electron dynamics.

Acknowledgements

We gratefully acknowledge the contributions of many co-workers and collaborators who have contributed to this work. In particular, we thank F. Remacle and B. Mignolet for their

calculations of strong-field-driven electron dynamics in ICCH⁺, A. Bandrauk and E. Penka-Fowe for time-dependent DFT calculations, O. Tolstikhin, L. Madsen, and T. Morishita for their calculations of strong-field ionization rates, A. Rupenyany and J. Schneider for their contributions to the experimental work, D. Baykusheva for calculations of impulsive alignment and orientation dynamics, L. Horny for extensive electronic-structure calculations, and G. Grassi for the synthesis of iodoacetylene. This work was financially supported by an ERC starting grant (project no. 307270-ATTOSCOPE) and the Swiss National Science Foundation (SNSF) via the National Center of Competence in Research Molecular Ultrafast Science and Technology. P.M.K. acknowledges support from the SNSF under project P2EZP2_165252.

Conflict of interest

The authors declare no conflict of interest.

- [1] A. Szabo, N. S. Ostlund, *Modern Quantum Chemistry: Introduction to Advanced Electronic Structure Theory*, Dover, New York, **1996**.
- [2] L. S. Cederbaum, W. Domcke, J. Schirmer, *Adv. Chem. Phys.* **1986**, *65*, 115.
- [3] J. Breidbach, L. S. Cederbaum, *J. Chem. Phys.* **2003**, *118*, 3983.
- [4] W. Von Niessen, G. Bieri, J. Schirmer, L. Cederbaum, *Chem. Phys.* **1982**, *65*, 157.
- [5] S. Lünemann, A. I. Kuleff, L. S. Cederbaum, *J. Chem. Phys.* **2008**, *129*, 104305.
- [6] G. S. Engel, et al., *Nature* **2007**, *446*, 782.
- [7] S. M. Falke, et al., *Science* **2014**, *344*, 1001.
- [8] T. Brixner, et al., *Nature* **2005**, *434*, 625.
- [9] P. Nuernberger, S. Ruetzel, T. Brixner, *Angew. Chem. Int. Ed.* **2015**, *54*, 11368; *Angew. Chem.* **2015**, *127*, 11526.
- [10] E. Romero, et al., *Nat. Phys.* **2014**, *10*, 676.
- [11] H.-G. Duan, et al., **2016**, <https://doi.org/10.1101/08425>.
- [12] I. Barth, J. Manz, *Angew. Chem. Int. Ed.* **2006**, *45*, 2962; *Angew. Chem.* **2006**, *118*, 3028.
- [13] M. Kanno, H. Kono, Y. Fujimura, *Angew. Chem. Int. Ed.* **2006**, *45*, 7995; *Angew. Chem.* **2006**, *118*, 8163.
- [14] T. Bredtman, J. Manz, *Angew. Chem. Int. Ed.* **2011**, *50*, 12652; *Angew. Chem.* **2011**, *123*, 12863.
- [15] I. Barth, J. Manz, Y. Shigeta, K. Yagi, *J. Am. Chem. Soc.* **2006**, *128*, 7043.
- [16] G. Sansone, T. Pfeifer, K. Simeonidis, A. I. Kuleff, *ChemPhys-Chem* **2012**, *13*, 661.
- [17] P. M. Paul, et al., *Science* **2001**, *292*, 1689.
- [18] M. Hentschel, et al., *Nature* **2001**, *414*, 509.
- [19] P. B. Corkum, F. Krausz, *Nat. Phys.* **2007**, *3*, 381.
- [20] F. Krausz, M. Ivanov, *Rev. Mod. Phys.* **2009**, *81*, 163.
- [21] "Attosecond Spectroscopy": H. J. Wörner, P. B. Corkum in *Handbook of High-Resolution Spectroscopy* (Eds.: M. Quack, F. Merkt), Wiley, New York, **2011**.
- [22] S. R. Leone, et al., *Nat. Photonics* **2014**, *8*, 162.
- [23] K. Ramasesha, S. R. Leone, D. M. Neumark, *Annu. Rev. Phys. Chem.* **2016**, *67*, 41.
- [24] S. R. Leone, D. M. Neumark, *Faraday Discuss.* **2016**, *194*, 15.
- [25] M. Drescher, et al., *Nature* **2002**, *419*, 803.
- [26] M. Uiberacker, et al., *Nature* **2007**, *446*, 627.
- [27] H. Wang, et al., *Phys. Rev. Lett.* **2010**, *105*, 143002.



- [28] B. Bernhardt, et al., *Phys. Rev. A* **2014**, *89*, 023408.
- [29] C. Ott, et al., *Nature* **2014**, *516*, 374.
- [30] G. Sansone, et al., *Nature* **2010**, *465*, 763.
- [31] F. Calegari, et al., *Science* **2014**, *346*, 336.
- [32] L. Belshaw, et al., *J. Phys. Chem. Lett.* **2012**, *3*, 3751.
- [33] F. Calegari, et al., *J. Phys. B* **2016**, *49*, 142001.
- [34] F. Calegari, G. Sansone, S. Stagira, C. Vozzi, M. Nisoli, *J. Phys. B* **2016**, *49*, 062001.
- [35] Z. H. Loh, et al., *Phys. Rev. Lett.* **2007**, *98*, 143601.
- [36] E. Goulielmakis, et al., *Nature* **2010**, *466*, 739.
- [37] A. Fleischer, et al., *Phys. Rev. Lett.* **2011**, *107*, 113003.
- [38] H. J. Wörner, P. B. Corkum, *J. Phys. B* **2011**, *44*, 041001.
- [39] L. Fechner, N. Camus, J. Ullrich, T. Pfeifer, R. Moshhammer, *Phys. Rev. Lett.* **2014**, *112*, 213001.
- [40] P. M. Kraus, et al., *Phys. Rev. Lett.* **2013**, *111*, 243005.
- [41] D. Baykusheva, P. M. Kraus, S. B. Zhang, N. Rohringer, H. J. Wörner, *Faraday Discuss.* **2014**, *171*, 113.
- [42] S. B. Zhang, D. Baykusheva, P. M. Kraus, H. J. Wörner, N. Rohringer, *Phys. Rev. A* **2015**, *91*, 023421.
- [43] H. Niikura, et al., *Nature* **2002**, *417*, 917.
- [44] H. Niikura, et al., *Nature* **2003**, *421*, 826.
- [45] J. L. Krause, K. J. Schafer, K. C. Kulander, *Phys. Rev. Lett.* **1992**, *68*, 3535.
- [46] P. B. Corkum, *Phys. Rev. Lett.* **1993**, *71*, 1994.
- [47] L. V. Keldysh, *Sov. Phys. JETP* **1965**, *20*, 1307.
- [48] M. Lein, *Phys. Rev. Lett.* **2005**, *94*, 053004.
- [49] S. Baker, et al., *Science* **2006**, *312*, 424.
- [50] S. Baker, et al., *Phys. Rev. Lett.* **2008**, *101*, 053901.
- [51] G. N. Gibson, R. R. Freeman, T. J. McIlrath, *Phys. Rev. Lett.* **1991**, *67*, 1230.
- [52] H. Akagi, et al., *Laser Phys.* **2009**, *19*, 1697.
- [53] X. Urbain, et al., *Phys. Rev. Lett.* **2004**, *92*, 163004.
- [54] H. J. Wörner, J. B. Bertrand, P. Hockett, P. B. Corkum, D. M. Villeneuve, *Phys. Rev. Lett.* **2010**, *104*, 233904.
- [55] R. Torres, et al., *Phys. Rev. A* **2010**, *81*, 051802.
- [56] P. M. Kraus, et al., *Science* **2015**, *350*, 790.
- [57] Y. Mairesse, et al., *Science* **2003**, *302*, 1540.
- [58] N. Dudovich, et al., *Nature Physics* **2006**, *2*, 781.
- [59] D. Shafir, et al., *Nature* **2012**, *485*, 343.
- [60] J. Zhao, M. Lein, *Phys. Rev. Lett.* **2013**, *111*, 043901.
- [61] M. Lein, P. P. Corso, J. P. Marangos, P. L. Knight, *Phys. Rev. A* **2003**, *67*, 023819.
- [62] J. Itatani, et al., *Nature* **2004**, *432*, 867.
- [63] T. Kanai, S. Minemoto, H. Sakai, *Nature* **2005**, *435*, 470.
- [64] S. Patchkovskii, Z. Zhao, T. Brabec, D. M. Villeneuve, *Phys. Rev. Lett.* **2006**, *97*, 123003.
- [65] S. Patchkovskii, Z. Zhao, T. Brabec, D. M. Villeneuve, *J. Chem. Phys.* **2007**, *126*, 114306.
- [66] R. Santra, A. Gordon, *Phys. Rev. Lett.* **2006**, *96*, 073906.
- [67] C. Vozzi, et al., *Nat. Phys.* **2011**, *7*, 822.
- [68] T. Morishita, A.-T. Le, Z. Chen, C. D. Lin, *Phys. Rev. Lett.* **2008**, *100*, 013903.
- [69] H. J. Wörner, H. Niikura, J. B. Bertrand, P. B. Corkum, D. M. Villeneuve, *Phys. Rev. Lett.* **2009**, *102*, 103901.
- [70] A.-T. Le, R. R. Lucchese, S. Tonzani, T. Morishita, C. D. Lin, *Phys. Rev. A* **2009**, *80*, 013401.
- [71] A. D. Shiner, et al., *Nat. Phys.* **2011**, *7*, 464.
- [72] S. Pabst, R. Santra, *Phys. Rev. Lett.* **2013**, *111*, 233005.
- [73] J. B. Bertrand, H. J. Wörner, P. Hockett, D. M. Villeneuve, P. B. Corkum, *Phys. Rev. Lett.* **2012**, *109*, 143001.
- [74] M. C. H. Wong, et al., *Phys. Rev. Lett.* **2013**, *110*, 033006.
- [75] A. Rupenyan, J. B. Bertrand, D. M. Villeneuve, H. J. Wörner, *Phys. Rev. Lett.* **2012**, *108*, 033903.
- [76] X. Ren, et al., *Phys. Rev. A* **2013**, *88*, 043421.
- [77] P. M. Kraus, D. Baykusheva, H. J. Wörner, *Phys. Rev. Lett.* **2014**, *113*, 023001.
- [78] P. M. Kraus, D. Baykusheva, H. J. Wörner, *J. Phys. B* **2014**, *47*, 124030.
- [79] C. Vozzi, et al., *Phys. Rev. Lett.* **2005**, *95*, 153902.
- [80] M. Lein, N. Hay, R. Velotta, J. Marangos, P. Knight, *Phys. Rev. Lett.* **2002**, *88*, 183903.
- [81] M. Lein, N. Hay, R. Velotta, J. P. Marangos, P. L. Knight, *Phys. Rev. A* **2002**, *66*, 023805.
- [82] O. Smirnova, et al., *Nature* **2009**, *460*, 972.
- [83] S. Haessler, et al., *Nat. Phys.* **2010**, *6*, 200.
- [84] R. Weinkauf, P. Schanen, D. Yang, S. Soukara, E. W. Schlag, *J. Phys. Chem.* **1995**, *99*, 11255.
- [85] R. Weinkauf, et al., *J. Phys. Chem.* **1996**, *100*, 18567.
- [86] R. Weinkauf, E. W. Schlag, T. J. Martinez, R. D. Levine, *J. Phys. Chem. A* **1997**, *101*, 7702.
- [87] L. Cederbaum, J. Zobeley, *Chem. Phys. Lett.* **1999**, *307*, 205.
- [88] F. Remacle, R. D. Levine, *Proc. Natl. Acad. Sci. USA* **2006**, *103*, 6793.
- [89] I. Fleming, *Molecular Orbitals and Organic Chemical Reactions*, Wiley, Hoboken, **2010**.
- [90] H. Hennig, J. Breidbach, L. S. Cederbaum, *J. Phys. Chem. A* **2005**, *109*, 409.
- [91] A. I. Kuleff, S. Lünemann, L. S. Cederbaum, *Chem. Phys.* **2013**, *414*, 100.
- [92] A. I. Kuleff, L. S. Cederbaum, *J. Phys. B* **2014**, *47*, 124002.
- [93] M. Lewenstein, P. Balcou, M. Y. Ivanov, A. L'Huillier, P. Corkum, *Phys. Rev. A* **1994**, *49*, 2117.
- [94] A. D. Shiner, et al., *Phys. Rev. Lett.* **2009**, *103*, 073902.
- [95] P. Salières, et al., *Science* **2001**, *292*, 902.
- [96] "Multielectron high harmonic generation: Simple man on a complex plane": O. Smirnova, M. Ivanov in *Attosecond and XUV Physics*, Wiley-VCH, Weinheim **2014**, pp. 201–256.
- [97] Y. Mairesse, et al., *Phys. Rev. Lett.* **2010**, *104*, 213601.
- [98] A. Etches, L. B. Madsen, *J. Phys. B* **2010**, *43*, 155602.
- [99] P. M. Kraus, et al., *Nat. Commun.* **2015**, *6*, 7039.
- [100] P. M. Kraus, H. J. Wörner, *ChemPhysChem* **2013**, *14*, 1445.
- [101] A.-T. Le, R. R. Lucchese, M. T. Lee, C. D. Lin, *Phys. Rev. Lett.* **2009**, *102*, 203001.
- [102] A.-T. Le, R. R. Lucchese, C. D. Lin, *Phys. Rev. A* **2010**, *82*, 023814.
- [103] C. Jin, et al., *J. Phys. B* **2011**, *44*, 095601.
- [104] C. Jin, et al., *Phys. Rev. A* **2012**, *85*, 013405.
- [105] A.-T. Le, R. R. Lucchese, C. D. Lin, *Phys. Rev. A* **2013**, *87*, 063406.
- [106] P. Colosimo, et al., *Nat. Phys.* **2008**, *4*, 386.
- [107] J. W. Cooper, *Phys. Rev.* **1962**, *128*, 681.
- [108] *VUV and Soft X-Ray Photoionization* (Eds.: U. Becker, D. A. Shirley), Plenum, New York, **1996**.
- [109] M. V. Frolov, N. L. Manakov, T. S. Sarantseva, A. F. Starace, *J. Phys. B* **2009**, *42*, 035601.
- [110] A. Rupenyan, P. M. Kraus, J. Schneider, H. J. Wörner, *Phys. Rev. A* **2013**, *87*, 033409.
- [111] A. Rupenyan, P. M. Kraus, J. Schneider, H. J. Wörner, *Phys. Rev. A* **2013**, *87*, 031401.
- [112] F. A. Gianturco, R. R. Lucchese, N. Sanna, *J. Chem. Phys.* **1994**, *100*, 6464.
- [113] A. P. P. Natalense, R. R. Lucchese, *J. Chem. Phys.* **1999**, *111*, 5344.
- [114] B. D. Bruner, et al., *Faraday Discuss.* **2016**, *194*, 369.
- [115] A.-T. Le, C. Lin, *J. Mod. Opt.* **2011**, *58*, 1158.
- [116] S. De et al., *Phys. Rev. Lett.* **2009**, *103*, 153002.
- [117] E. Frumker, et al., *Phys. Rev. Lett.* **2012**, *109*, 113901.
- [118] P. M. Kraus, A. Rupenyan, H. J. Wörner, *Phys. Rev. Lett.* **2012**, *109*, 233903.
- [119] E. F. Penka, E. Couture-Bienvenue, A. D. Bandrauk, *Phys. Rev. A* **2014**, *89*, 023414.
- [120] O. I. Tolstikhin, T. Morishita, L. B. Madsen, *Phys. Rev. A* **2011**, *84*, 053423.

- [121] O. I. Tolstikhin, T. Morishita, *Phys. Rev. A* **2012**, *86*, 043417.
[122] L. B. Madsen, O. I. Tolstikhin, T. Morishita, *Phys. Rev. A* **2012**, *85*, 053404.
[123] L. B. Madsen, F. Jensen, O. I. Tolstikhin, T. Morishita, *Phys. Rev. A* **2013**, *87*, 013406.
[124] O. I. Tolstikhin, L. B. Madsen, T. Morishita, *Phys. Rev. A* **2014**, *89*, 013421.
[125] M. Allan, E. Kloster-Jensen, J. P. Maier, *J. Chem. Soc. Faraday Trans. 2* **1977**, *73*, 1406.
[126] X. Zhou, et al., *Phys. Rev. Lett.* **2008**, *100*, 073902.
[127] J. Levesque, D. Zeidler, J. P. Marangos, P. B. Corkum, D. M. Villeneuve, *Phys. Rev. Lett.* **2007**, *98*, 183903.
[128] X. Zhou, et al., *Phys. Rev. Lett.* **2009**, *102*, 073902.
[129] N. Rohringer, R. Santra, *Phys. Rev. A* **2009**, *79*, 053402.
[130] A. Wirth, et al., *Science* **2011**, *334*, 195.
[131] S. Pabst, M. Lein, H. J. Wörner, *Phys. Rev. A* **2016**, *93*, 023412.
[132] H. Vincenti, F. Quéré, *Phys. Rev. Lett.* **2012**, *108*, 113904.
[133] J. A. Wheeler, et al., *Nat. Photonics* **2012**, *6*, 829.
[134] K. T. Kim, et al., *Nat. Photonics* **2013**, *7*, 651.
[135] F. Quéré, et al., *J. Phys. B* **2014**, *47*, 124004.
[136] F. Silva, S. M. Teichmann, S. L. Cousin, M. Hemmer, J. Biegert, *Nat. Commun.* **2015**, *6*, 6611.
[137] C. Zhang, G. Vampa, D. Villeneuve, P. Corkum, *J. Phys. B* **2015**, *48*, 061001.
[138] T. Hammond, K. T. Kim, C. Zhang, D. Villeneuve, P. Corkum, *Opt. Lett.* **2015**, *40*, 1768.
[139] D. Shafir, Y. Mairesse, D. M. Villeneuve, P. B. Corkum, N. Dudovich, *Nat. Phys.* **2009**, *5*, 412.
[140] J. M. Dahlström, A. L'Huillier, J. Mauritsson, *J. Phys. B* **2011**, *44*, 095602.
[141] H. Yun, et al., *Phys. Rev. Lett.* **2015**, *114*, 153901.
[142] G. Vampa, et al., *Nature* **2015**, *522*, 462.
[143] A. Fleischer, O. Kfir, T. Diskin, P. Sidorenko, O. Cohen, *Nat. Photonics* **2014**, *8*, 543.
[144] O. Kfir, et al., *Nat. Photonics* **2015**, *9*, 99.
[145] D. Baykusheva, M. S. Ahsan, N. Lin, H. J. Wörner, *Phys. Rev. Lett.* **2016**, *116*, 123001.
[146] W. Boutu, et al., *Nat. Phys.* **2008**, *4*, 545.
[147] M. Huppert, I. Jordan, D. Baykusheva, A. von Conta, H. J. Wörner, *Phys. Rev. Lett.* **2016**, *117*, 093001.
[148] R. Kienberger, et al., *Nature* **2004**, *427*, 817.
[149] E. Goulielmakis, et al., *Science* **2004**, *305*, 1267.
[150] E. Goulielmakis, et al., *Science* **2008**, *320*, 1614.
[151] M. Schultze, et al., *Science* **2010**, *328*, 1658.
[152] M. Sabbar, et al., *Phys. Rev. Lett.* **2015**, *115*, 133001.
[153] T. Kanai, E. J. Takahashi, Y. Nabekawa, K. Midorikawa, *Phys. Rev. Lett.* **2007**, *98*, 153904.
[154] J. B. Bertrand, H. J. Wörner, P. Salières, D. M. Villeneuve, P. B. Corkum, *Nat. Phys.* **2013**, *9*, 174.
[155] G. Gademann, et al., *New J. Phys.* **2011**, *13*, 033002.
[156] J. Leeuwenburgh, B. Cooper, V. Averbukh, J. P. Marangos, M. Ivanov, *Phys. Rev. Lett.* **2013**, *111*, 123002; D. Azoury et al., *Nat. Commun.* **2017**, *8*, 1453.
[157] J. Breidbach, L. S. Cederbaum, *Phys. Rev. Lett.* **2005**, *94*, 033901.
[158] M. Ossiander, et al., *Nat. Phys.* **2017**, *13*, 280.
[159] S. G. Walt, N. B. Ram, N. Atala, N. Shvetsov-Shilovski, A. von Conta, D. Baykusheva, M. Lein, H. J. Wörner, *Nat. Commun.* **2017**, *8*, 15651.
[160] For a recent review, see: H. J. Wörner et al., *Struct. Dynamics* **2017**, *4*, 061508.
[161] D. Baykusheva, S. Brennecke, M. Lein, H. J. Wörner, *Phys. Rev. Lett.* **2017**, *119*, 203201.

Manuscript received: March 16, 2017

Revised manuscript received: May 29, 2017

Accepted manuscript online: July 5, 2017

Version of record online: ■ ■ ■ ■ ■ ■ ■ ■ ■ ■

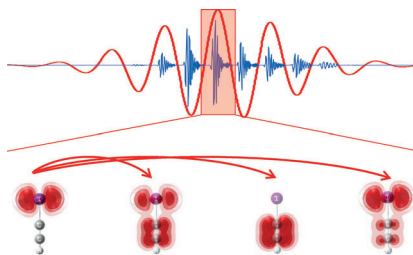
Reviews

Spectroscopic Methods

P. M. Kraus,*

H. J. Wörner* ————— ■■■■-■■■■

Perspectives of Attosecond Spectroscopy
for the Understanding of Fundamental
Electron Correlations



The concept of molecular orbitals, one of the most successful in chemistry, commonly fails if strong electron correlation is present. This Review shows how high-harmonic generation, the process for generating attosecond pulses in the extreme ultraviolet, can be used to spectroscopically access electron dynamics in molecules following ionization, and how the technique could be extended to identify the effects of electron correlation on dynamics.